The Thesis Committee for Emre Yavuz
Certifies that this is the approved version of the following thesis:

The Construction and Use of Plasticity Models to Predict Elevated Temperature Forming of Magnesium ZEK100 Alloy Sheet Material

APPROVED BY
SUPERVISING COMMITTEE:

Supervisor:

Eric M. Taleff

David L. Bourell

The Construction and Use of Plasticity Models to Predict Elevated Temperature Forming of Magnesium ZEK100 Alloy Sheet Material

by

Emre Yavuz, B.Sc.

Thesis

Presented to the Faculty of the Graduate School of

The University of Texas at Austin

in Partial Fulfillment

of the Requirements

for the Degree of

Master of Science in Engineering

The University of Texas at Austin

August, 2014

Dedication

To my lovely wife Gamze Yavuz,

and my valued family.

Acknowledgements

I thank my advisor, Dr. Eric M. Taleff, for his guidance, insight and support during my graduate studies.

I thank Turkish Petroleum Corporation (TPAO) for their support during my graduate studies.

I thank Dr Aravindha Antoniswamy for his help with experimental work, discussions, teaching and guidance. I thank Philip Noel for his help in interpretation. I thank the other (past and present) members of my research group, Dr. Trevor Watt, Thomas Ivanoff, Andrew Weldon and Dr Nicholas Pedrazas.

Finally, I thank my lovely wife, Gamze Yavuz and my beloved joint-family in Turkey for their support during the time that I spent here.

Abstract

The Construction and Use of Plasticity Models to Predict Elevated Temperature Forming of Magnesium ZEK100 Alloy Sheet Material

Emre Yavuz, M.S.E

The University of Texas at Austin, 2014

Supervisor: Eric M. Taleff

Magnesium (Mg) alloys provide material properties that make them attractive for structural components. In particular Mg alloys can be used to produce components with lighter weight than most alloy sheets currently used. However, the insufficient ductility of Mg alloy sheet materials at room temperature can require these to be formed at elevated temperatures to achieve suitable formability. In this research, wrought Mg alloy ZEK100 is studied at 300 °C and lower temperatures. Behavior at these lower temperatures is compared to behavior of 450 °C and 350 °C. A goal of this study is to determine the possibilities for future forming technologies at these lower temperatures. The deformation mechanisms at these temperatures are examined, including their relation to plastic anisotropy. Knowledge of the active deformation mechanisms is used to formulate descriptive models of plastic deformation. Material constitutive models are constructed and used in finite element method (FEM) simulations of gas pressure bulge tests. Finally,

results of FEM simulations are compared with experimental results, and the accuracies of the material constitutive models are validated.

Table of Contents

List of Tables

List of Figures

Chapter 1: Introduction

Magnesium (Mg) is the fourth most abundant element in the Earth behind iron, oxygen and silicon [1]. It is one of the most commonly used metals. Ions of magnesium are easily soluble in water, seawater contains 0.13% Mg by mass [1]. Thus, seawater is an important source of Mg. Another important feature of Mg is that it is recyclable.

Starting from the 21st century, a new oil crisis began to appear in the world. Because vehicles are a main consumer of fuel and oil, the automotive and aerospace industries aimed to find different ways to save fuel. One of the most efficient ways to decrease fuel consumption is to decrease the total mass of vehicles. To decrease mass, light-weighting alloys have been investigated. Since Mg is one of these potentially useful light-weighting materials, researchers recently focused on various Mg alloys. The low density of Mg alloys makes them attractive to the automobile and aerospace industries. Mg alloys have lower density than other metals used in these industries, such as aluminum (Al) and steel. The density of Mg is approximately two-thirds that of aluminum and one-fourth that of steel. Because of these advantages, researchers are looking for possible replacements of Al and steel with Mg alloys [2-7].

Mg alloys are considered for possible material replacements to reduce increasing environmental problems. Decreasing the total mass of vehicles will reduce green-house gas emissions [3-6].

Among the Mg alloys, ZEK100 has many advantages over other more common Mg alloys, such as AZ31. Better room-temperature ductility than AZ31 is one example of these advantages. The composition of ZEK100 includes 1% Zn, 0.2 % Nd, 0.2% Zr and a balance of Mg, by weight. Since ZEK100 includes rare-earth elements, it has a weaker basal texture than AZ31 [2]. This weaker basal texture provides better room-temperature

ductility than AZ31. ZEK100 was studied before at temperatures close to those used in the commercial Quick Plastic Forming (QPF) process, 450°C, by Aravindha Antoniswamy [3]. However, the ductility of ZEK100 was not previously investigated for temperatures from 300°C to room temperature (22°C). In this study, deformation behavior of ZEK100 alloy sheet is studied at temperatures from 22 °C to 300 °C. Data obtained are compared with the data of Aravindha Antoniswamy [3].

To understand the effects of temperature and strain rate on formability of ZEK100, experimental tests were performed. Uniaxial tensile tests were conducted at The University of Texas at Austin laboratories with a computer controlled servohydraulic test frame system (MTS 810). Tests were conducted for different strain rates at temperatures from 300°C to 22°C. By using the results of uniaxial tensile tests, material constitutive models were created [3, 8-9]. These models were used in finite-element-method (FEM) simulations. Forming of ZEK100 alloy sheet was simulated at different temperatures and pressures. By using the results of FEM simulations, dome height *versus* time and thickness *versus* time predictions were obtained. The results of FEM simulations were compared with the results of experimental biaxial bulge forming experiments. Related plots were created for these comparisons. These plots were used to understand the validity of material constitutive models. According to the results of these comparisons, the accuracies of material constitutive models were determined [8, 9].

REFERENCES

1. "Science Safety: Chapter 8". Government of Manitoba. Retrieved 2007-08-21, “www.edu.gov.mb.ca/k12/docs/support/scisafe/chapter8. html”.

2. A.J. Carpenter, “Physics-Based Material Constitutive Models for the Simulation of High-Temperature Forming of Magnesium Alloy AZ31,” PhD Thesis, University of Texas at Austin, (2012).
3. A.R. Antoniswamy, “The Construction and Use of Physics-Based Plasticity Models and Forming-Limit Diagrams to Predict Elevated Temperature Forming of Three Magnesium Alloy Sheet Materials,” PhD Thesis, University of Texas at Austin, (2013).
4. L.H. Pomeroy: Automotive Engineering, 1922, vol. XI, no. 6, pp. 508-519.
5. G.S. Cole, A.M. Sherman: Mater. Char., 1995, vol. 35, pp. 3-9.
6. J.J. Lee, S.P. Lukachko, I.A. Waitz, A. Schafer: Annual Review of Energy and the Environment, 2001, vol. 26, pp. 167-200.
7. A.I. Taub: *MRS Bulletin*, 2006, vol. 31, pp. 336-343.
8. J.A. Yasi, L.G. Hector, Jr., D.R. Trinkle: *Acta Mater.*, 2011, vol. 59, pp. 5652-60.
9. A.J. Carpenter, A.R. Antoniswamy, J.T. Carter, L.G. Hector, Jr., E.M. Taleff, A Grain-size Dependent Material Constitutive Model for the Hot Deformation of Mg AZ31B Sheet at 450°C, (2014), *Acta Materialia*.

Chapter 2: Literature Review

2.1. Magnesium Alloys, Properties and Performance

Mg alloys possess many attractive properties, such as low density. Because of these attractive properties, Mg alloys are intriguing to the automobile and aerospace industries. Researchers also attach importance to Mg alloys. Although Mg ZEK100 is a new material, several reports on it are available in the literature [1, 2, 6, 25, 26, 27]. Reports and studies on other Mg alloys, such as WE43 [3], ZK60 [4, 5], AZ31 [6, 8], are present as well. In this section, literature on Mg ZEK100 alloy sheet is reviewed.

The low density of Mg alloys brings with it potential for light weighting. Usage of light-weight alloys is desired by the automobile and aerospace industries to decrease the total mass of vehicles. These industries aim to use Mg alloys in their products to decrease fuel consumption and increase performance. It is also desired to decrease green-house gas emissions by using Mg alloys. However, manufacturers must consider the strength and the stiffness of these materials before using them. Any new material must meet all the required properties for any application. For the automobile industry, the parts produced from Mg alloys must resist yielding and deflection. While making weight-reduction comparisons, these features must be considered and evaluated together [7]. To this purpose, Luo et al. [9] created a performance chart by using the material performance index, M. They used M to describe the performance of different materials. Al AA5182, Mg AZ31 and the steel were compared in that study. To be able to compare all these three materials at equal bending strength and equal bending stiffness, material thickness was accepted as a free variable. The result of that study is shown in Table 2.1. Properties of Mg ZEK100, from Ref. 28, were also added to Table 2.1. Thus, all these four materials are compared. As can be seen from the data, Mg ZEK100 alloy sheet might be an attractive replacement for Al and steel.

Table 2.1: Comparison of Mg AZ31, Mg ZEK100, Al AA5182 and Steel. This table shows that Mg ZEK100 might be a possible replacement for Al and steel. Data are from Ref. 9. (*) data from Ref. 28.

Material	Density (g/cm^3)	Yield Strength (MPa)	Elastic Modulus (GPa)	Mass Ratio (equal bending stiffness)	Mass Ratio (equal bending strength)
Mg AZ31	1.77	220	45	0.38	0.22
Mg ZEK100(*)	1.75	218	45	0.37	0.22
Al AA5182	2.68	235	70	0.50	0.32
Steel	7.80	200	210	1	1

The room-temperature formability of a material can be partly understood through the Lankford coefficient, R. The plastic anisotropy of a material is quantified in the R-value. During forming, sheet metal resists thinning when the R-value is high. This resistance to thinning behavior is a result of the plastic anisotropy of the material. Generally, larger R values provide better formability at room temperature. However, a high R-value is not necessarily an advantage in sheet forming at elevated temperature, for which resistance to thinning is typically controlled by the material's strain-rate sensitivity. With the help of R values, plastic anisotropy of materials is compared. Equation 1 shows the calculation of the R value [6]. In this equation t_0 is the initial thickness, t is the final thickness, w_0 is the initial width and w is the final width [6]. To calculate an accurate R value, at least five different locations are measured for each specimen. The thickness and the width of the specimen are measured at these five locations, and an R value is calculated at each. The average of the R-values at these five locations is the R-value reported.

$$R = \frac{\epsilon_w}{\epsilon_t} = \frac{\log\left(\frac{w_0}{w}\right)}{\log\left(\frac{t_0}{t}\right)} \qquad (1)$$

By measuring R-values, plastic anisotropies of ZEK100, AZ31B-HR and AZ31B-H24 are compared at room temperature [11]. As a result, it was found that ZEK100 shows less plastic anisotropy than the Mg AZ31 alloys. It is assumed that this is a result of the weaker basal texture of ZEK100 [6]. Since Mg ZEK100 includes rare-earth elements in its composition, it has a weaker texture than Mg AZ31 alloys in sheet form [6, 11]. This research also suggests that Mg ZEK100 might be an attractive replacement for Mg AZ31 alloys.

The formabilities of ZEK100 and AZ31 were compared by Boba et al. [12] from room temperature to 300°C. For all temperatures, it was observed that ZEK100 provides better formability than AZ31. Antoniswamy [6] compared ductilities at elevated temperatures from 300°C to 450°C and observed that ZEK100 still provides better formability [6]. These researchers demonstrated that Mg ZEK100 alloy sheet generally has better formability than Mg AZ31 alloys. Because of that, ZEK100 might be formed at lower temperatures than Mg AZ31. Thus several advantages, such as easier part handling and energy savings, might be obtained.

2.2. HIGH TEMPERATURE FORMING OF MG ALLOYS

Although Mg alloys have several properties superior to Al and steel, they have lower formabilities at room temperature. This is a significant obstacle to the use of Mg alloys. This disadvantage can be overcome by forming at high temperatures, at which sufficient ductility can be achieved. Figure 2.1 shows the results from Antoniswamy [6] for ZEK100 tested at 350°C and 450 °C. As seen in Figure 2.1, the ductility of ZEK100 increases with increasing temperature from 350 °C to 450 °C.

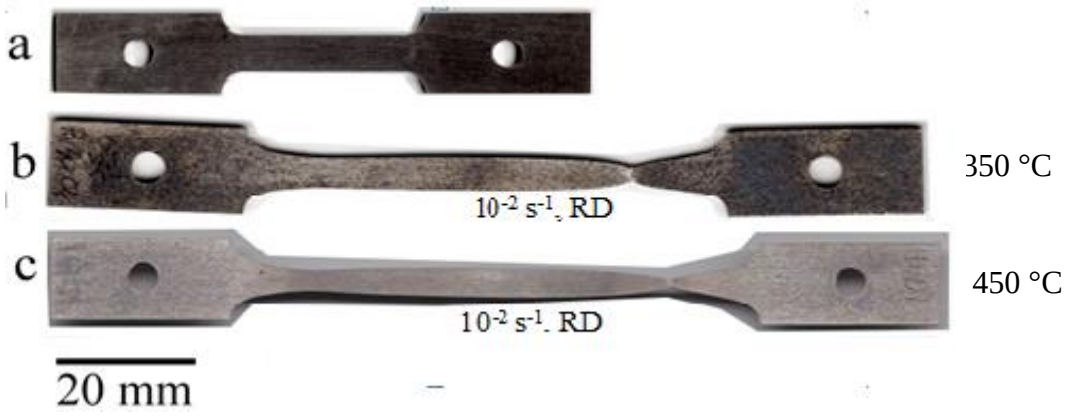

Figure 2.1: Tensile test specimens are shown with the tensile direction parallel to the RD for (a) an untested specimen, (b) a tensile specimen tested to rupture at 350°C and 10^{-2} s^{-1} and (c) a tensile specimen tested to rupture at 450°C and 10^{-2} s^{-1}. This figure is from Ref. 6.

Insufficient ductility of Mg alloys can be solved by forming at elevated temperatures. The Taylor criterion explains the reason for inadequate ductility of Mg alloys at low temperatures. According to the Taylor criterion, a ductile material must have at least five independent slip systems [6, 14]. Mg has an hexagonal-close-packed (HCP) crystal structure [8]. At room temperature, there are only two independent slip systems active, both are basal slip systems, for Mg alloys. With increasing temperature, the critical resolved shear stress of other slip systems decreases [6, 8, 14]. Thus it becomes easier to overcome the critical resolved shear stress of other slip systems, such as prismatic slip, and activate more slip systems [8]. Then, the ductility of Mg alloys increases as well. Because of this, commercial forming of Mg alloys can be conducted at elevated temperatures (450°C) [6].

2.3. MATERIAL CONSTITUTIVE MODELS

Deformation mechanisms in materials are defined by using material constitutive models. To create material constitutive models, uniaxial tension test results, stress-strain

data, are used. Deformation behaviors of a material can be predicted by an accurate material model. To validate the accuracy of a material model, the created model is used in a finite-element-model (FEM) simulation. The results of the FEM simulations are compared with the results of independent biaxial bulge tests. According to the results of this comparison, modifications can be made to the material constitutive model. In literature there are multiple material constitutive models for the high temperature deformation behavior of Mg alloys. However, almost all of these models are designed as single-term models that consider only one active creep mechanism [16 – 20].

In recent years, researchers showed that the deformation in AZ31Mg alloy sheet is controlled by two creep mechanisms at high temperatures. One of these studies was conducted by Sherek et al. [21]. Sherek et al. [21] studied the deformation of AZ31B-H24 alloy sheet at 450 ^{o}C. They generated a new model that included both dislocation-climb (DC) creep and grain-boundary-sliding (GBS) creep [6]. However, this new model did not consider normal anisotropy under DC creep [6, 21]. Thus, biaxial bulge forming at fast strain rates could not be predicted well using this model [6]. In this model, equation 2, $\dot{\varepsilon}$ is the strain rate from both creep mechanisms together, σ is flow stress, A_1 and n_1 are functions of strain, ε, that describe GBS creep; and A_2 and n_2 are constant values that describe five-power dislocation creep [6, 21, 22].

$$\dot{\varepsilon} = A_1(\varepsilon)\sigma^{n_1(\varepsilon)} + A_2\sigma^{n_2} \quad (2)$$

Another model was created by Taleff et al. [23] in 2010. Their model covered the deficiency of the previous models in literature. They found that GBS creep controls the deformation mechanisms at high temperatures and slow strain rates. However, DC creep becomes active at low temperatures and fast strain rates. Taleff et al. [23] considered both

of these conditions while they were creating the new model. Equation 3 shows the model improved by Taleff et al. [23], where T is temperature, $\dot{\varepsilon}$ is true-strain rate, E is the elastic modulus of magnesium, σ is true stress, R is the ideal gas constant, A_{GBS}, n_{GBS}, and Q_{GBS} are constant values of the GBS creep, and A_{DC}, n_{DC}, and Q_{DC} are constant values of the DC creep. In this equation, the first term shows the contribution from GBS creep and the second term shows the contribution from DC creep. To predict an accurate true strain rate, both the GBS and DC creep terms are added to each other [23].

$$\dot{\varepsilon} = A_{GBS}\left(\frac{\sigma}{E}\right)^{n_{GBS}} \exp\left(-\frac{Q_{GBS}}{RT}\right) + A_{DC}\left(\frac{\sigma}{E}\right)^{n_{DC}} \exp\left(-\frac{Q_{DC}}{RT}\right) \quad (3)$$

Recently, another model was developed by Carpenter et al. [8]. Carpenter et al. [8] improved the model of Sherek et al. [21]. Their model also included two creep mechanisms for Mg alloys. This model considered the grain growth and normal anisotropy of the material as well. The new model is shown for a constant temperature in equation 4, where $\dot{\varepsilon}$ is the true strain rate, σ is the true stress, $A_{GBS}(\varepsilon)$ is the pre-exponential factor for GBS creep, A_{DC} is the pre-exponential factor for DC creep, n_{GBS} and n_{DC}, are the stress exponents [8]. The validity of this model was proved by Antoniswamy [6] and Carpenter et al. [8] in their studies about MgAZ31 alloy sheet.

$$\dot{\varepsilon} = A_{GBS}(\varepsilon)\sigma^{n_{GBS}(\varepsilon)} + A_{DC}\sigma(\varepsilon)^{n_{DC}} \quad (4)$$

Antoniswamy [6] also studied the deformation mechanisms of Mg ZEK100 alloy sheet at elevated temperatures. Antoniswamy [6] used the model developed by Carpenter et al. [8] for Mg ZEK100 alloy sheet as well. However, the deformation of Mg ZEK100

alloy sheet is controlled by only DC creep at high temperatures. Furthermore, depending on the temperature, lattice self-diffusion and/or pipe diffusion controls the DC creep mechanism of ZEK100 alloy sheet. To consider all of these effects together, Antoniswamy [6] modified the previous model as shown in equation 5 [6]. In this equation for a constant temperature, σ is the true stress, $A_{DC(l)}$ is the pre-exponential factor for lattice self-diffusion controlled DC creep, $A_{DC(p)}$ is the pre-exponential factor for pipe-diffusion controlled DC creep, $n_{DC(l)}$, and $n_{DC(p)}$ are the stress exponents [6]. The validity of this model was proved by Antoniswamy [6] by running FEM simulation of ZEK100 alloy sheet at 350 °C and 450 °C.

$$\dot{\varepsilon} = A_{DC(l)}\sigma(\varepsilon)^{n_{DC(l)}} + A_{DC(p)}\sigma(\varepsilon)^{n_{DC(p)}} \quad (5)$$

REFERENCES

1. S. Kurukuri, D.G. Tari, M.J. Worswick, R.K. Mishra, J.T. Carter, "Dynamic Characterization of AZ31B and ZEK100 Magnesium Alloy Sheets," International Conference on Magnesium Alloys and their Applications, W.J. Poole, K.U. Kainer, eds., Vancouver, Canada, 2012.
2. M. Boba, M.J. Worswick, R.K. Mishra, J.T. Carter, "Formability of AZ31B and ZEK100 Magnesium Alloy Sheets at Elevated Temperatures," International Conference on Magnesium Alloys and their Applications, W.J. Poole, K.U. Kainer, eds., Vancouver, Canada, 2012.
3. J. Gao, Q. Wang, Y. Wang, W. Li, W. Niu, "Microstructure and Kinetics of Hot Deformation WE43 Magnesium Alloy," Rare Metals, 27(2008), pp. 405-409.

4. A. Galiyev, R. Kaibyshev, G. Gottstein, “Correlation of Plastic Deformation and Dynamic Recrystallization in Magnesium Alloy ZK60,” Acta Materialia, 49(2001), pp. 1199-1207.
5. A. Bussiba, A. Ben Artzy, A. Shtechman, S. Ifergan, M. Kupiec, “Grain Refinement of AZ31 and ZK60 Mg alloys - Towards Superplasticity Studies,” Materials Science and Engineering A, 302 (2001), pp. 56-62.
6. A.R. Antoniswamy, “The Construction and Use of Physics-Based Plasticity Models and Forming-Limit Diagrams to Predict Elevated Temperature Forming of Three Magnesium Alloy Sheet Materials,” PhD Thesis, University of Texas at Austin, (2013).
7. ASM: Metals Handbook, Vol. 20, Materials Park, OH, 2002.
8. A.J. Carpenter, “Physics-Based Material Constitutive Models for the Simulation of High-Temperature Forming of Magnesium Alloy AZ31,” PhD Thesis, University of Texas at Austin, (2012).
9. A.A. Luo: JOM, 2002, vol. 54, no. 2, pp. 42-48.
10. J. Min, Y. Cao, J.T. Carter, R. Verma, “Comparison of Tensile Properties and Crystallographic Textures of Three Magnesium Alloy Sheets,” Magnesium Technology, S.M. Mathaudhu, W.H. Sillekens, N.R. Neelameggham , N.Hort, eds., TMS (2012), pp. 355-360.
11. J. Bohlen, M. R. Nürnberg, J.W. Senn, D. Letzig, S.R. Agnew, “The Texture and Anisotropy of Magnesium–zinc–rare Earth Alloy Sheets,” Acta Materialia, 55 (2007), pp. 2101-2112.
12. M. Boba, M.J. Worswick, R.K. Mishra, J.T. Carter, “Formabiltiy of A31B and ZEK100 Magnesium Alloy Sheets at Elevated Temperatures,” International

Conference on Magnesium Alloys and their Applications, W.J. Poole, K.U. Kainer, eds., Vancouver, Canada, 2012.

13. 13. M.W. Toaz, E.J. Ripling: J. Met., 1956, vol. 8, pp. 936-946.Birbilis, N.; Williams, G.; Gusieva, K.; Samaniego, A.; Gibson, M. A.; McMurray, H. N. (2013). "Poisoning the corrosion of magnesium". Electrochemistry Communications 34: 295. doi:10.1016/j.elecom.2013.07.021
14. G.S. Cole, A.M. Sherman: Mater. Char., 1995, vol. 35, pp. 3-9.
15. "Science Safety: Chapter 8". Government of Manitoba. Retrieved 2007-08-21.
16. H.-K. Kim, W.-J. Kim, Creep Behavior of AZ31 Magnesium Alloy at Low Temperature Range between 423 K and 473 K, J. Mater. Sci., 2007, 42(15) , pp. 6171-6176.
17. I.A. Maksoud, H. Ahmed, J. Rödel, Investigation of the Effect of Strain Rate and Temperature on the Deformability and Microstructure Evolution of AZ31 Magnesium Alloy, Mater. Sci. Eng. A, 2009, 504(1), pp. 40-48.
18. S. Spigarelli, M. El Mehtedi, Creep as an Extension of Hot Working: A Unified Approach to High Temperature Deformation of AZ31 Alloy, Mater. Sci. Eng. A, 2010, 527(21), pp. 5708-5714.
19. C. Bruni, L. Donati, M. El Mehtedi, M. Simoncini, Constitutive Models for AZ31 Magnesium Alloys, Key Eng. Mater., 2008, 367, pp. 87-94.
20. U.F. Kocks, C.N. Tome, H.-R. Wenk (Eds.), “Texture and Anisotropy,” Cambridge, New York (2000), pp. 204-206.
21. P.A. Sherek, A.J. Carpenter, L.G. Hector, Jr., P.E. Krajewski, J.T. Carter, J. Lasceski, E.M. Taleff, “The Effects of Strain and Stress State in Hot Forming of Mg AZ31 Sheet,” *Magnesium Technology*, S.M. Mathaudhu, W.H. Sillekens, N.R. Neelameggham , N.Hort, eds., TMS (2012), pp. 301-306.

22. Alexander J. Carpenter, Eric M. Taleff, Louis G. Hector, Jr., Jon T. Carter, and Paul E. Krajewski. "A Time-Dependent Material Model for the Simulation of Hot Gas-Pressure Forming of Magnesium Alloy AZ31." *Materials Science Forum*, 735 (2013), pp. 198-203.
23. E.M. Taleff, L.G. Hector, Jr., R. Verma, P.E. Krajewski, J.-K. Chang: J. Mater. Eng. Perform., 2010, vol. 19, pp. 488-94.
24. F.K. Abu-Farha, M.K. Khraisheh: Adv. Eng. Mater., 2007, vol. 9, no. 9, pp. 777-83.
25. J. Min, J. Lin: Anelastic Behavior and Phenomenological Modelling of Mg ZEK100-O Alloy Sheet Under Cyclic Tensile Loading – Unloading, Mater. Sci. Eng. A, 2013, pp. 174 – 182.
26. I. Aslam, B. Li, Z. McClelland, S.J. Horstemeyer, Q. Ma, P.T. Wang, M.F. Horstemeyer: Three Point Bending Behavior of a ZEK100 Mg Alloy at Room Temperature, Mater. Sci. Eng. A 590, pp. 168-173.
27. J. Min, J. Lin, J. Li: Forming Limits of Mg Alloy ZEK100 Sheet in Perform Annealing Process, (2013).
28. M. Alderman: The Lightest Structural Metal in Automotive, Niche Vehicle Network, (2013).

Chapter 3: Objectives and Methodology

3.1. Research Objectives

In this research, tests were conducted on a ZEK100 alloy sheet at 300 °C, 250 °C, 200 °C, 100 °C, and room temperature (22°C) under strain rates from $3x10^{-4}$ to 10^{-1} s^{-1} to identify the deformation mechanisms in this material. To identify these mechanisms, it is necessary to complete uniaxial tension tests at different temperatures and strain rates and biaxial bulge tests at different temperatures and pressures. The data from these tests were analyzed to create informative plots. The results of uniaxial tension tests were used to create material constitutive models. To determine the accuracy of these material models, FEM simulations were used. The results of FEM simulations were compared to the results of experimental biaxial bulge tests for model validation. Using the results of these comparisons, the material models were modified as needed. Eventually, the accuracy of the material constitutive models were validated.

3.2. Research Methodologies

For this research, the methodology shown in Figure 3.1 was used. The purpose of this methodology is to construct and validate material constitutive models for ZEK100 alloy sheet. First of all, uniaxial tensile tests were completed to collect stress – strain data. All the tests were conducted at The University of Texas at Austin laboratories. Figure 3.2 shows the uniaxial tension test machine in The University of Texas at Austin laboratories. Before beginning each test, a three-zone resistance furnace was heated to the desired temperature. All the tests were completed at the desired test temperature. Before and during the tensile tests K-type thermocouples were used to measure the temperature of the tensile specimen. Thus, temperature was controlled, and all the tests were completed with temperature controlled to within ±2.0 °C of the desired temperature. At the end of

each tension test, the specimen was quenched immediately to preserve the microstructure for possible future analysis.

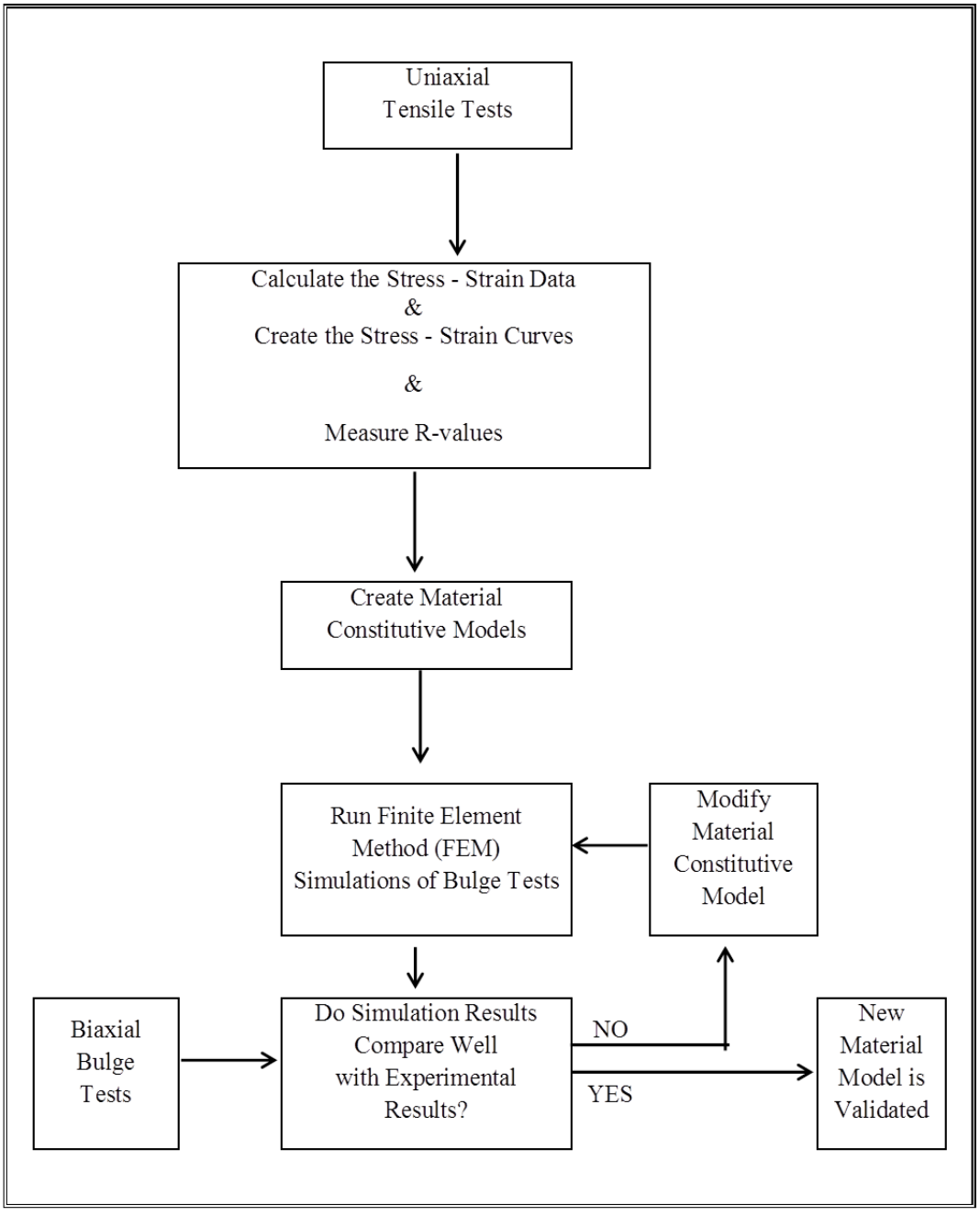

Figure 3.1: The methodology followed in this study to create and validate new material constitutive models [1, 2].

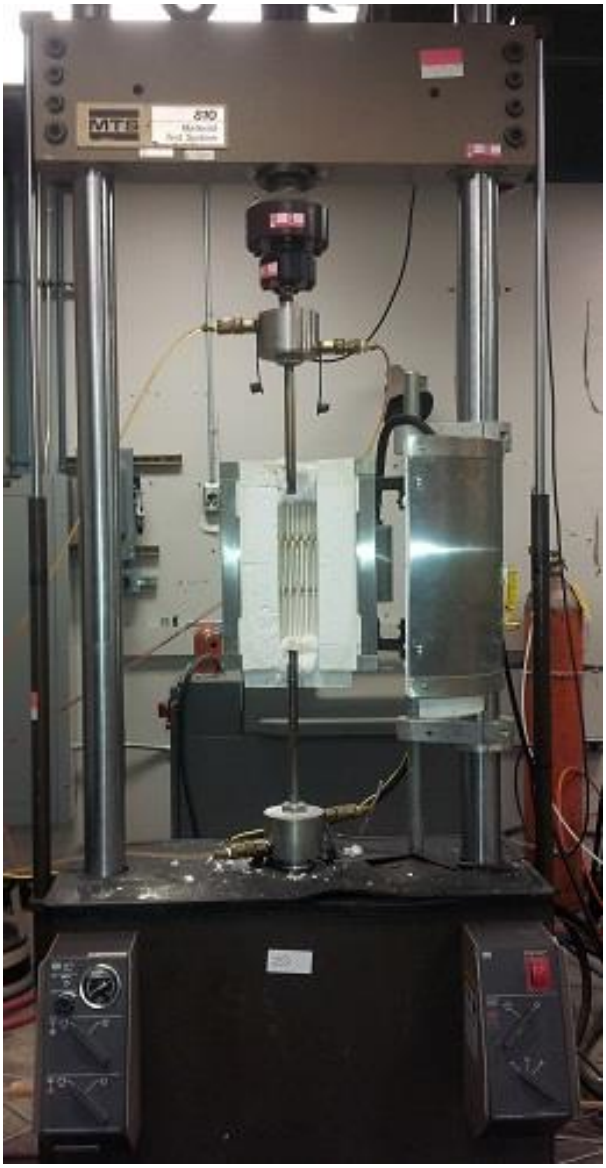

Figure 3.2: Tension test machine in The University of Texas at Austin laboratories

Figure 3.3: Biaxial bulge test machine in The University of Texas at Austin laboratories

A computer-controlled servohydraulic test frame was used to perform uniaxial tension tests. By analyzing the raw data of these tests, stress – strain curves were created. Width and thickness of each tested tensile specimen were measured from at least five different locations. By using these measurements, R-values were calculated. Stress- strain data and the R-value calculations were used to create mathematical models for material tested at different temperatures. These models were applied to ABAQUS^{TM} FEM

simulations of bulge-forming experiments. To obtain experimental data against which simulation predictions could be compared experimental biaxial bulge tests were also completed. Figure 3.3 shows the biaxial bulge test machine in The University of Texas at Austin laboratories. Before biaxial bulge testing, the test furnace was preheated to the desired temperature. Then a specimen was mounted in the test machine. Before starting a test, the specimen was heated to the desired temperature for approximately one minute. The temperature of each specimen was measured by K-type thermocouples before and during the test. To form the sheet, a prearranged gas pressure was applied to the specimen from a bottle of compressed nitrogen (N_2) gas. Figure 3.4 shows the mechanism of the biaxial bulge test machine and a picture of a tested specimen.

a

b

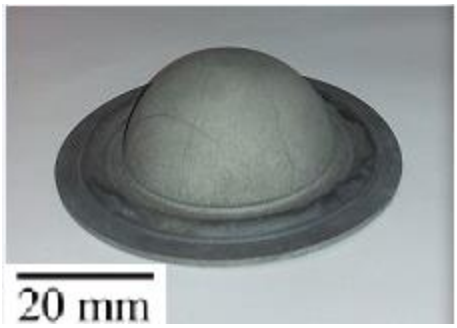

Figure 3.4: Photographs show (a) the biaxial bulge test die holders in the furnace and (b) a specimen after the test was completed.

Simulation results were compared against the experimental data to verify the applied material model. Results of these comparisons were examined to correct and modify the models. Formabilities at the different temperatures were compared. From the result of these comparisons, needed graphs were created. On the graphs, data from the current study and the previous studies were compared.

REFERENCES

1. A.J. Carpenter, "Physics-Based Material Constitutive Models for the Simulation of High-Temperature Forming of Magnesium Alloy AZ31," PhD Thesis, University of Texas at Austin, (2012).
2. A.R. Antoniswamy, "The Construction and Use of Physics-Based Plasticity Models and Forming-Limit Diagrams to Predict Elevated Temperature Forming of Three Magnesium Alloy Sheet Materials," PhD Thesis, University of Texas at Austin, (2013).

Chapter 4: Material and Experimental Methods

4.1. MATERIAL, ZEK100 ALLOY SHEET

One of the greatest disadvantages of Mg alloys is low formability. Due to their HCP crystal structure, Mg alloys do not have enough active slip systems at low temperatures to achieve high ductility [1, 3, 4, 6]. As mentioned in Chapter 2, this inadequate number of active slip systems does not satisfy the Taylor criterion. The strong basal texture of many Mg alloy sheet materials further reduces ductility at low temperatures. To achieve ductilities equivalent to those of steels and Al alloys, Mg alloys must be formed at elevated temperatures. However, Mg ZEK100 contains rare-earth elements. Because of these rare-earth elements, ZEK100 has a weaker basal texture than most other Mg alloys. Thus, ZEK100 might be formed at lower temperatures than the other Mg alloys. Forming at lower temperatures generally produces more energy savings, better surface quality and easier part handling [2, 3, 5]. These potential advantages of ZEK100 are of interest to further explore.

In this study, forming of ZEK100 was examined at elevated temperatures. ZEK100 was investigated at temperatures below the commercial forming temperature used in the QPF process (450 °C). Tests were conducted on a ZEK100 alloy sheet at 300 °C, 250 °C, 200 °C, 100 °C and room temperature (22°C). Results of these tests were compared with those Antoniswamy [3]. The formabilities of ZEK100 were evaluated across a wide range of temperatures. For these tests, sheet material with a thickness of 1.56 mm was used. For each test temperature, tests were conducted at six true-strain rates, ranging from 3×10^{-4} s^{-1} to 10^{-1} s^{-1}. All the test results were compared.

4.2. EXPERIMENTAL PROCEDURE

Automobile and aerospace industries aim to use Mg alloys in their products for light weighting. However, the low formability of Mg alloys is an obstacle to their use. Thus, it is proposed to determine the best forming conditions for Mg alloys. For this purpose, the R-values were investigated at different temperatures and strain rates to measure plastic anisotropy. To understand the effects of temperature and strain rate on the R-value, several uniaxial tension tests were conducted at temperatures from 300 °C to room temperature (22 °C) for strain rates from 3×10^{-4} s^{-1} to 10^{-1} s^{-1}. Tensile tests were conducted with the tensile direction (TD) parallel to the long transverse direction (LTD), parallel to the rolling direction (RD) and at 45^0 to LTD and RD directions.

4.2.1 Tensile Tests

Figure 4.1 shows an untested dog-bone shaped specimen used for tensile testing. Specimens were machined using a water-jet machine in The University of Texas at Austin Mechanical Engineering machine shop. Specimens were machined with three different tensile directions: TD parallel to LTD, RD and 45^0. The gage length of each specimen was 25 mm, with a gage width of 6 mm, a shoulder radius of 3.2 mm and a gage thickness of 1.56 mm. Tests were conducted at The University of Texas at Austin Laboratories. A photograph of the tensile test system is shown as Figure 3.2.

Figure 4.1: An untested ZEK100 tensile coupon is shown.

Before testing each specimen, the dimensions of the specimen were measured using calipers. The furnace was preheated to the desired temperature before testing. Temperature was measured using K-type thermocouples. When the furnace reached the desired temperature, a test specimen was mounted in the furnace. The temperature of the specimen was measured at two locations in its gage region during the test. Thus temperature was controlled, and a uniform temperature was obtained to within ±2.0°C of the desired temperature. Depending on the test temperatures, preheating times varied from 19 to 30 minutes.

Tensile tests were first conducted until rupture for the specimens in the LTD orientation. These tests were conducted at five different temperatures; 300 °C, 250 °C, 200 °C, 100 °C and 22 °C, for constant true-strain rates of $3x10^{-4}$, 10^{-3}, 10^{-2} and 10^{-1} s^{-1}. To be able to understand better the strain rate effect on ductility, two more tests were conducted at strain rates of $3x10^{-3}$ and $3x10^{-2}$ s^{-1} for the temperature of 300 °C. By using the results of these tests, stress-strain curves were created, and R values were calculated. Figure 4.2 shows specimens tested until rupture for different strain rates at 300 °C.

To obtain more dependable R-value measurements, fixed-strain tests were performed at 300 °C, 250 °C, 200 °C, 100 °C for LTD, RD and 45^0 oriented specimens to a true strain of approximately 0.2. For the LTD specimens, tests were also performed at room temperature. Through fixed strain tests, the effects of specimen orientation on forming were evaluated by comparing test data from RD, LTD and 45^0 orientations. These comparisons will be shown in Chapter 5 in detail.

Figure 4.2: Specimens with the TD parallel to LTD, tested at a temperature of 300°C. The tested specimens demonstrate a diffuse neck.

R-value calculations were performed using the specimen thickness and width measurements. After tests were completed, the final width and thickness of each specimen were measured at 5 different locations along the gauge length. For each specimen, R-values were calculated at these five locations. The average of these five values is reported here as the R-value. R-values were measured from both specimens tested until rupture and to a fixed-strain of ε=0.2. Since rupture tests were affected by necking, fixed-strain tests were used to calculate the reported R-values. R-value measurements were explained in detail at Chapter 2.

The uniaxial tension data contained displacement, force and time data. By using these data, engineering stress-strain and true stress-strain data were calculated. These calculated data were used to create related plots for each temperature and strain rate. These plots will be compared with each other and previous studies in Chapter 5 and 6.

4.2.2 Biaxial Bulge Tests

Biaxial bulge tests were performed to obtain experimental data of forming dome height *versus* time. It was desired to use these data to make comparison with finite-element-method (FEM) simulation results, thus testing material constitutive models.

Biaxial bulge tests were performed at The University of Texas at Austin laboratories. Figure 3.3 shows the testing machine located at The University of Texas at Austin. For these tests, specimens with a 90 mm diameter and a 1.56 mm thickness were used. Tests were conducted at 300 °C for five different gas pressures, ranging from 300 psi to 380 psi.

Before testing, the furnace was preheated to the desired test temperature. Before and during the tests, K-type thermocouples were used to measure the temperature of the furnace and specimen. Temperature was controlled to within ±2.0°C of the desired test

temperature. After the furnace reached the desired test temperature, a specimen was mounted in the testing system. Then the upper and lower dies of the machine were clamped together. To form the specimen, a constant gas pressure was applied. The height of the dome formed was measured with a digital micrometer. Tests were run until the dome height reached approximately 20 mm. For 300 °C the forming time varied from approximately 1000 sec to 4000 sec, depending on the applied pressure. Figure 3.3 shows the die holders of the biaxial bulge test machine and the final picture of the specimen after a test was completed.

REFERENCES

1. J. Min, J. Lin: Anelastic Behavior and Phenomenological Modelling of Mg ZEK100-O Alloy Sheet Under Cyclic Tensile Loading – Unloading, Mater. Sci. Eng. A, 2013, pp. 174 – 182.
2. H. M. Rao, R. I. Rodrigez, J. B. Jordon, M. E. Barkey, Y. B. Guo, H. Badarinarayan, W. Yuan, Friction Stir Spot Welding of Rare-Earth Containing ZEK100 Magnesium Alloy Sheets, Material and Design 56 (2014), pp. 750-754.
3. A.R. Antoniswamy, "The Construction and Use of Physics-Based Plasticity Models and Forming-Limit Diagrams to Predict Elevated Temperature Forming of Three Magnesium Alloy Sheet Materials," PhD Thesis, University of Texas at Austin, (2013).
4. A.J. Carpenter, "Physics-Based Material Constitutive Models for the Simulation of High-Temperature Forming of Magnesium Alloy AZ31," PhD Thesis, University of Texas at Austin, (2012).

5. R.R. Craig, Jr.: Mechanics of Materials, 3rd ed., Hoboken: John Wiley & Sons, 2011, pp. 37-45.
6. G.I. Taylor: J. Inst. Metals, 1938, vol. 62, pp. 307–24.

Chapter 5: Experimental Results

5.1. TENSILE DATA

Figures 5.1 – 5.5 show the strain rate effect on ductility while temperature was constant. Tests were conducted for LTD parallel TD at five constant temperatures from 300 °C to 22 °C for strain rates ranging from 10^{-1} to $3x10^{-4}$ s^{-1}. At 300 °C, tests were conducted for six different strain rates of 10^{-1} s^{-1}, $3x10^{-1}$ s^{-1}, 10^{-2} s^{-1}, $3x10^{-2}$ s^{-1}, 10^{-3} s^{-1} and $3x10^{-4}$ s^{-1}. For temperatures from 22 to 250^{0}C, tests were conducted for four different strain rates of 10^{-1} s^{-1}, 10^{-2} s^{-1}, 10^{-3} s^{-1} and $3x10^{-4}$ s^{-1}. Related plots were created by using the results of these tests. As can be seen from the figures, ductility generally increases with decreasing strain rate for all temperatures. For all temperatures, flow stress increases with increasing strain rate. This evidences a positive strain-rate sensitivity [1]. Necking was observed in all the specimens tested at temperatures from 300 °C to 100 °C. For the specimens tested at room temperature, necking was not observed.

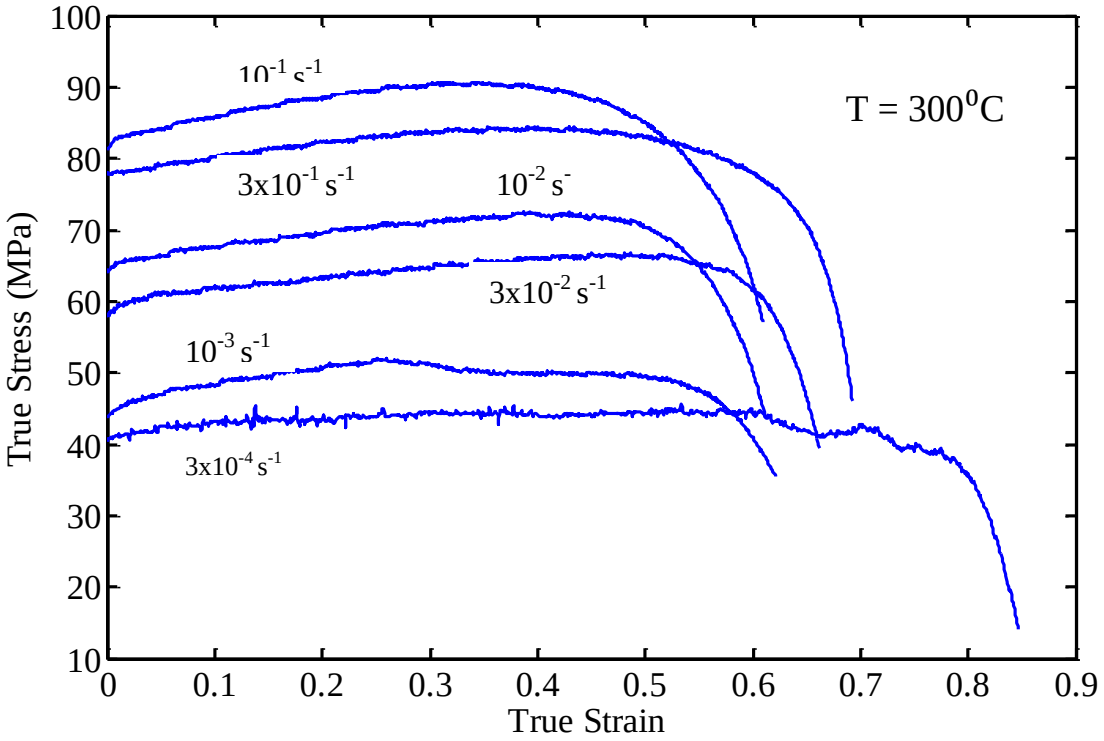

Figure 5.1: For TD parallel to LTD specimens, tensile data at 300°C and six strain rates of 3×10^{-1} s^{-1}, 10^{-1} s^{-1}, 3×10^{-2} s^{-1}, 10^{-2} s^{-1}, 10^{-3} s^{-1} and 3×10^{-4} s^{-1} are shown.

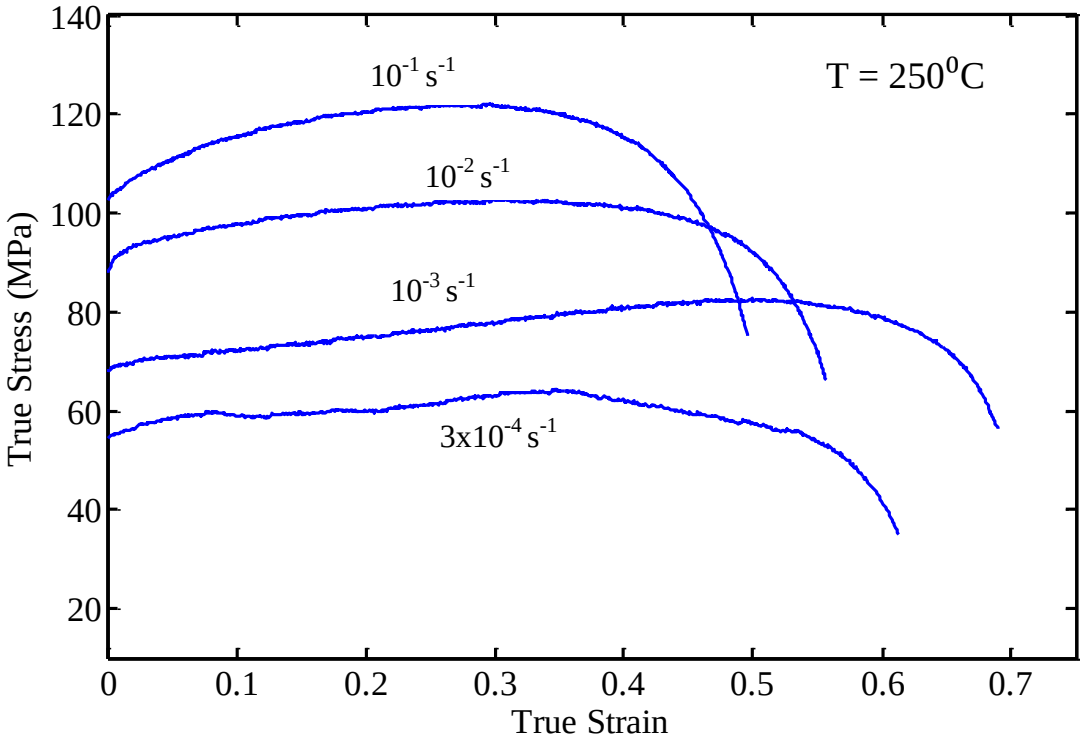

Figure 5.2: For TD parallel to LTD specimens, tensile data at 250°C and four strain rates of 10^{-1} s^{-1}, 10^{-2} s^{-1}, 10^{-3} s^{-1} and 3×10^{-4} s^{-1} are shown.

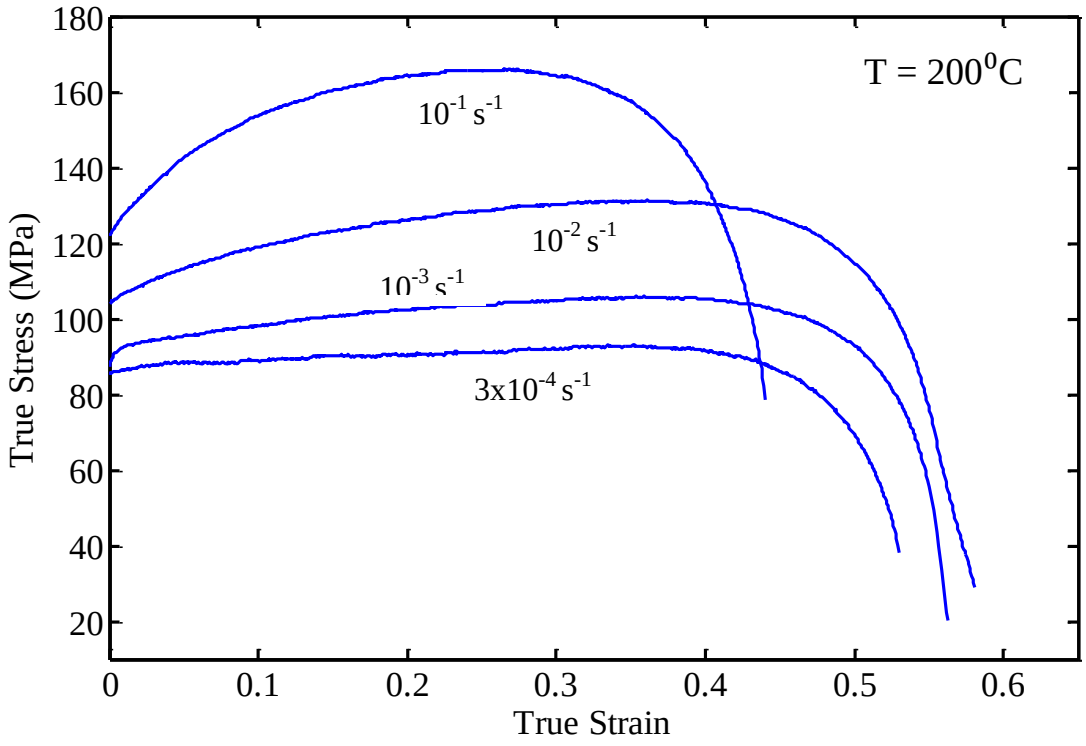

Figure 5.3: For TD parallel to LTD specimens, tensile data at 200°C and four strain rates of 10^{-1} s^{-1}, 10^{-2} s^{-1}, 10^{-3} s^{-1} and 3×10^{-4} $s^{-1}$are shown.

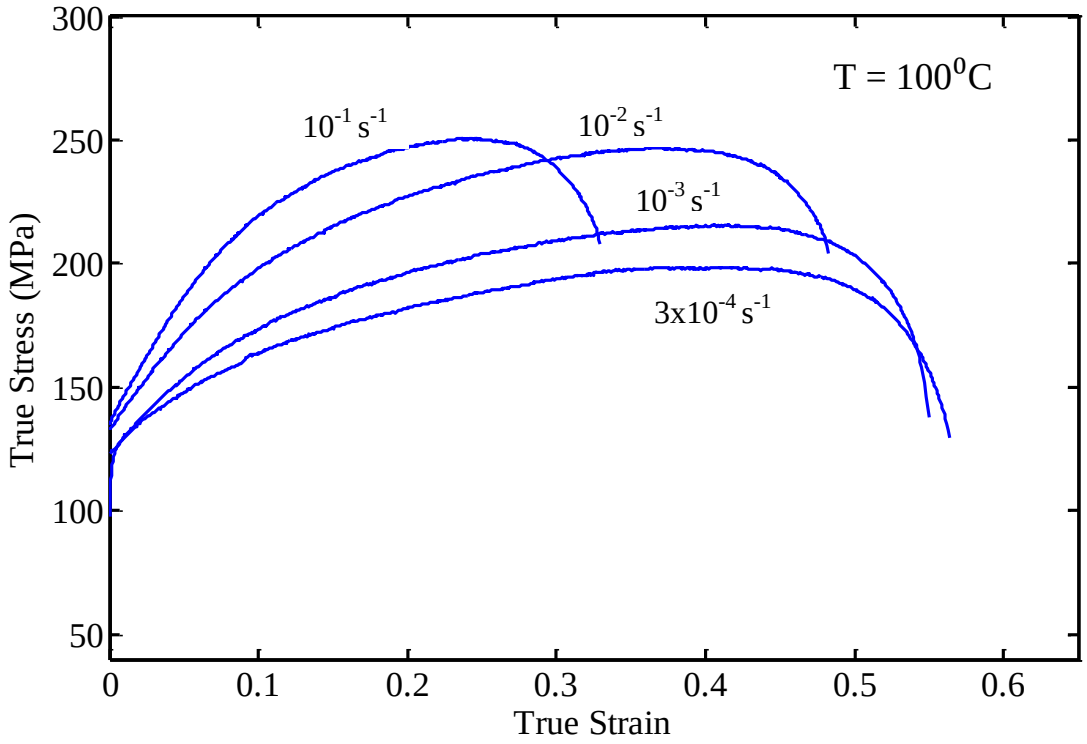

Figure 5.4: For TD parallel to LTD specimens, tensile data at 100°C and four strain rates of 10^{-1} s^{-1}, 10^{-2} s^{-1}, 10^{-3} s^{-1} and 3×10^{-4} $s^{-1}$are shown.

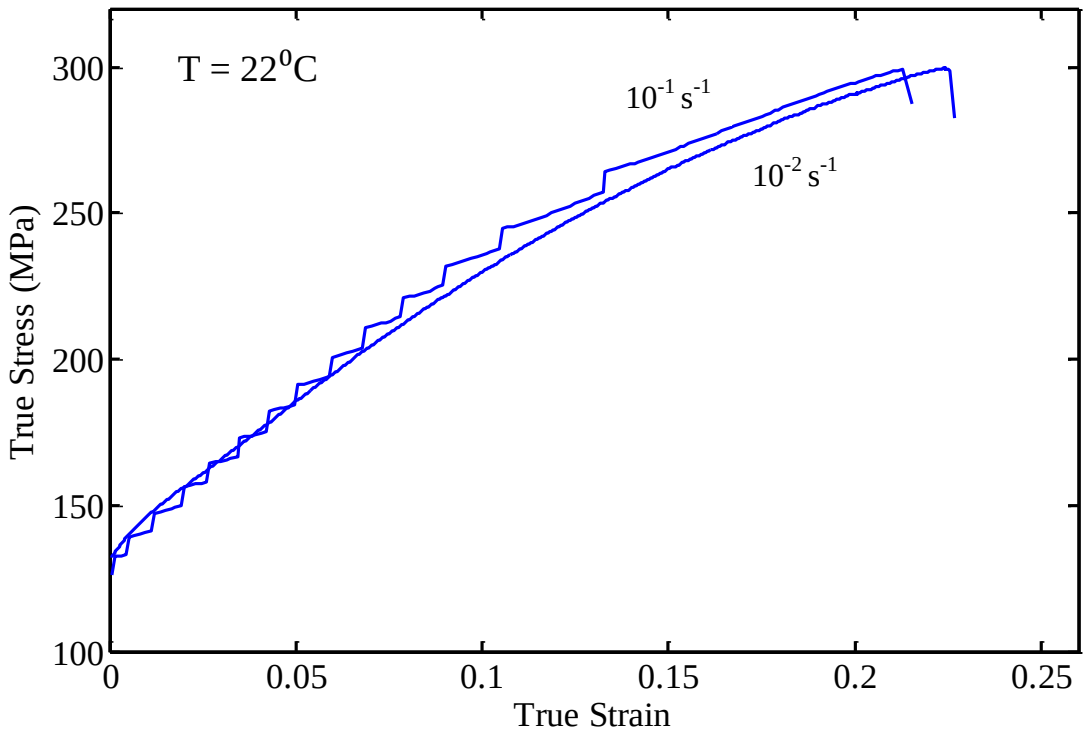

Figure 5.5: For TD parallel to LTD specimens, tensile data at room temperature (22°C) and two strain rates of 10^{-1} s^{-1} and 10^{-2} s^{-1} are shown.

Figures 4.1, 5.6 – 5.9 also show the strain rate effect on ductility. The ductility increases with decreasing strain rate. These figures show the tensile specimens, TD parallel to LTD, tested at strain rates from 10^{-1} to $3x10^{-4}$ s^{-1} and temperatures from 300 °C to 22°C. It can be seen from the figures that all the tested specimens show necking, except for the specimens tested at room temperature.

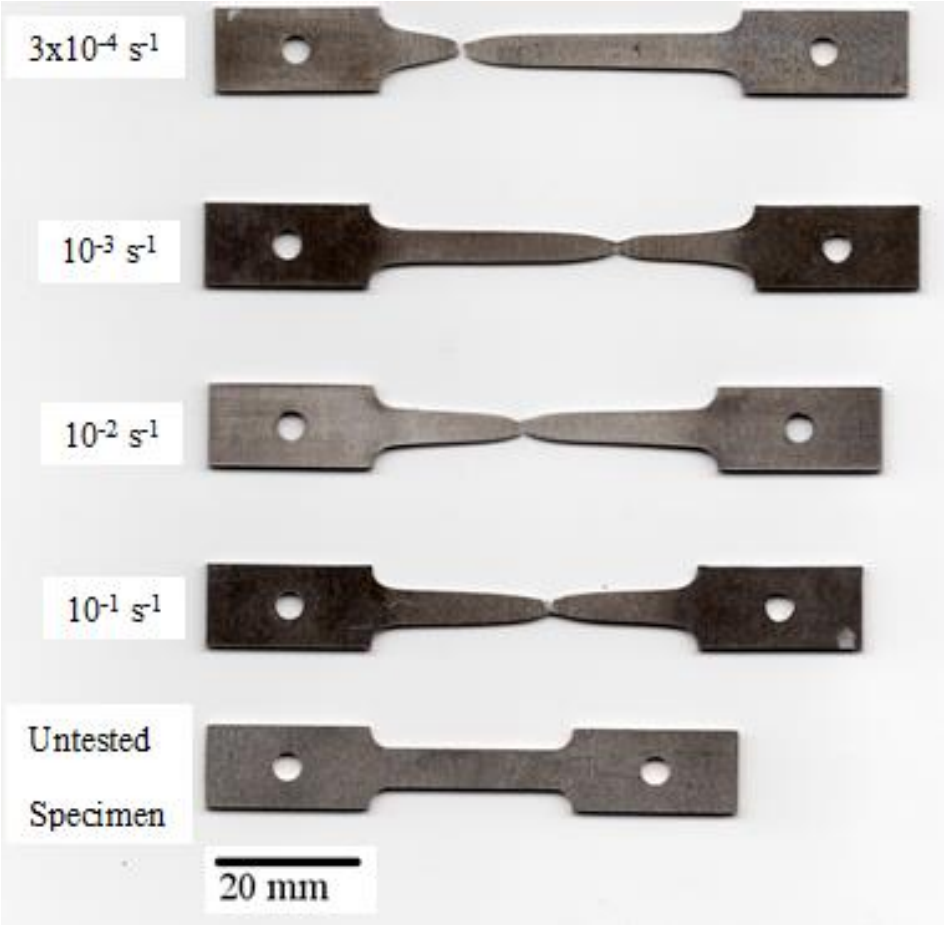

Figure 5.6: Specimens with TD parallel to LTD tested at a temperature of 250°C. The tested specimens demonstrate diffuse necks.

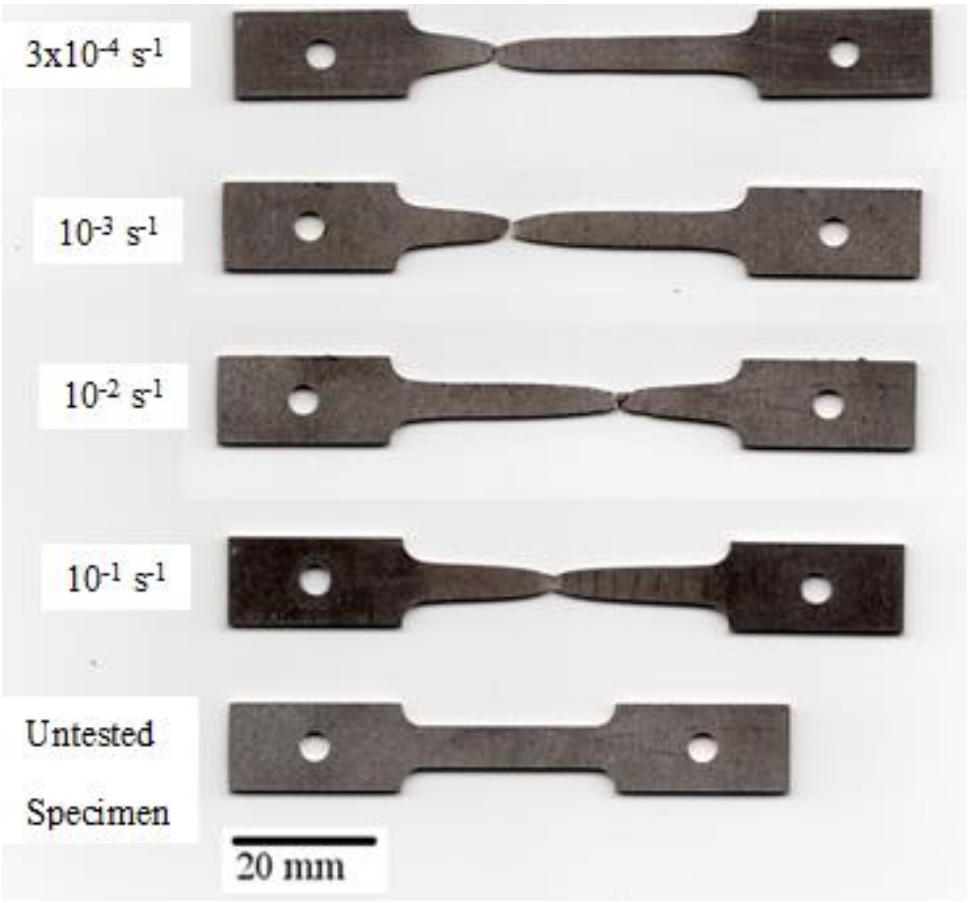

Figure 5.7: Specimens with TD parallel to LTD tested at a temperature of 200°C. The tested specimens demonstrate diffuse necks.

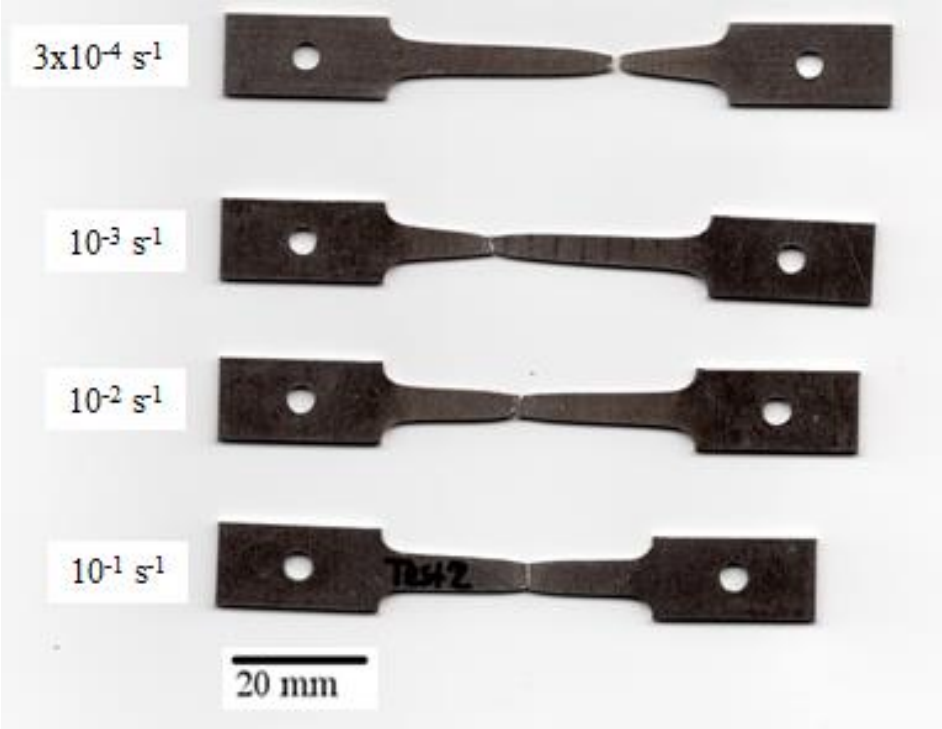

Figure 5.8: Specimens with TD parallel to LTD tested at a temperature of 100°C. The tested specimens demonstrate diffuse necks.

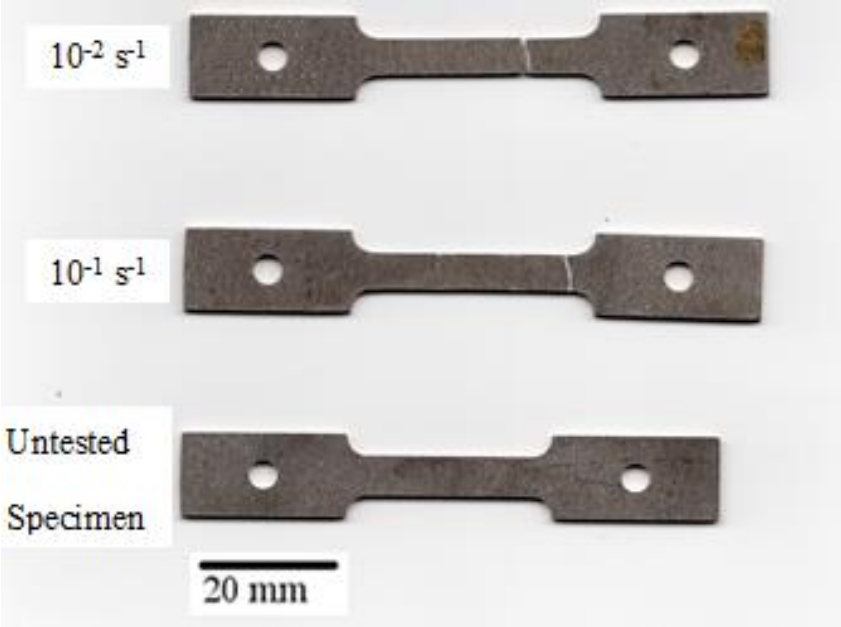

Figure 5.9: Specimens with TD parallel to LTD tested at a temperature of 22°C.

Figures 5.10 – 13 show the temperature effect on ductility while strain rate is constant. Tests were conducted with TD parallel to LTD at temperatures from 22 to 300°C. Each figure shows data at a constant strain rate from 10^{-1} to $3x10^{-4}$ s^{-1}. For all strain rates, the maximum stress obtained decreases as temperature increases. As seen in the figures, strain at rupture increases with increasing temperature for all temperatures at strain rates of 10^{-1} and 10^{-2} s^{-1}. At strain rates of 10^{-3} and $3x10^{-4}$ s^{-1}, strain at rupture increases only between 200 °C and 300 °C.

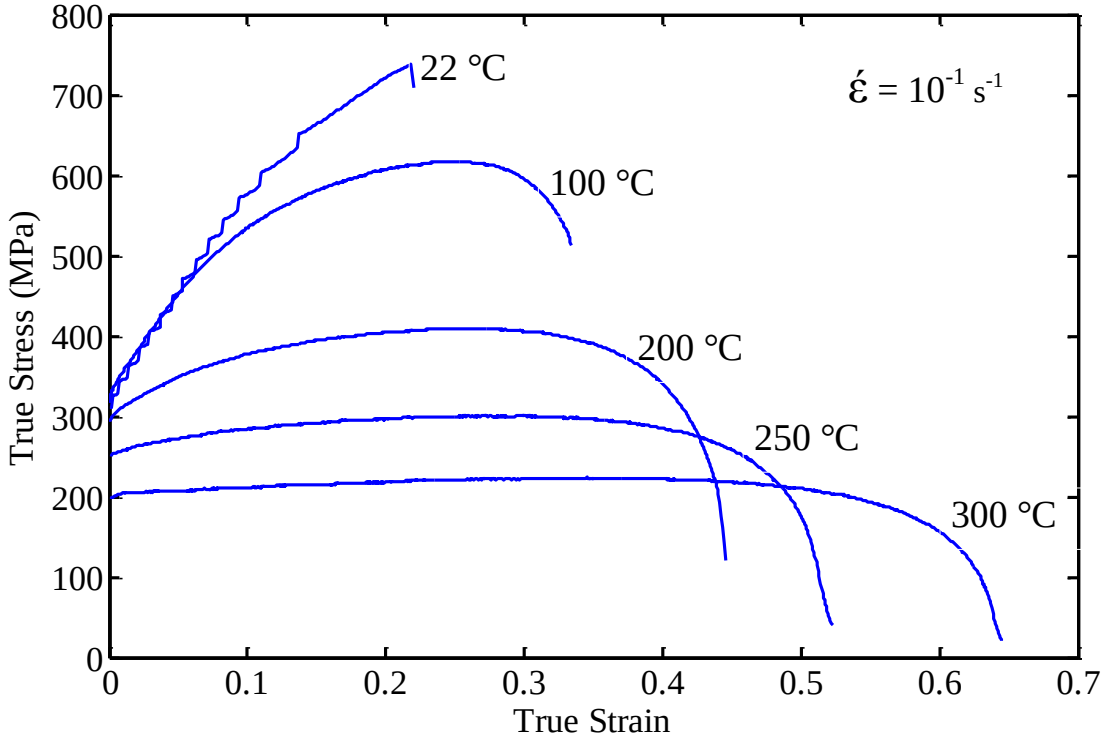

Figure 5.10: Specimens tested at a constant true-strain rate of 10^{-1} s^{-1} and the temperatures of room temperature (22°C), 100°C, 200°C, 250°C and 300°C are shown for TD parallel to the LTD. With increasing temperature, stress decreases and strain at rupture increases.

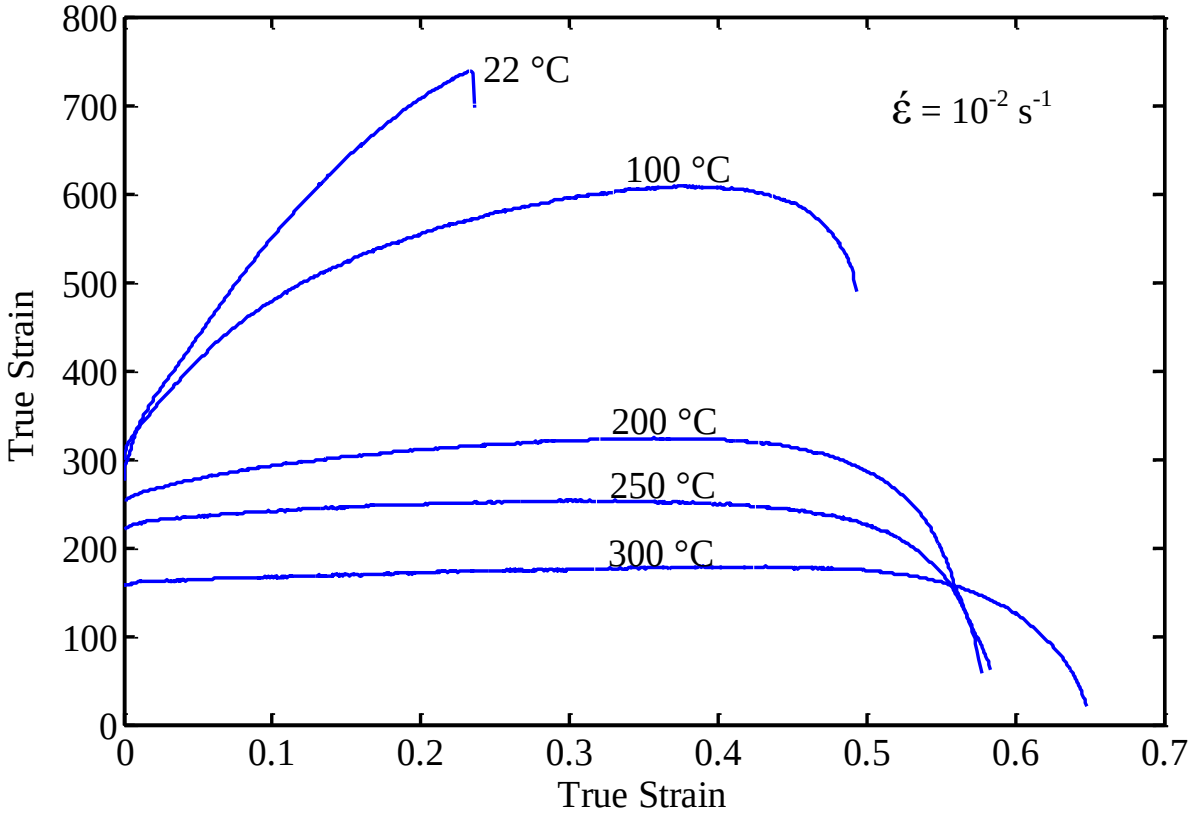

Figure 5.11: Specimens tested at a constant true-strain rate of 10^{-2} s^{-1} and the temperatures of room temperature (22°C), 100°C, 200°C, 250°C and 300°C are shown for TD parallel to the LTD. With increasing temperature, stress decreases and strain at rupture increases.

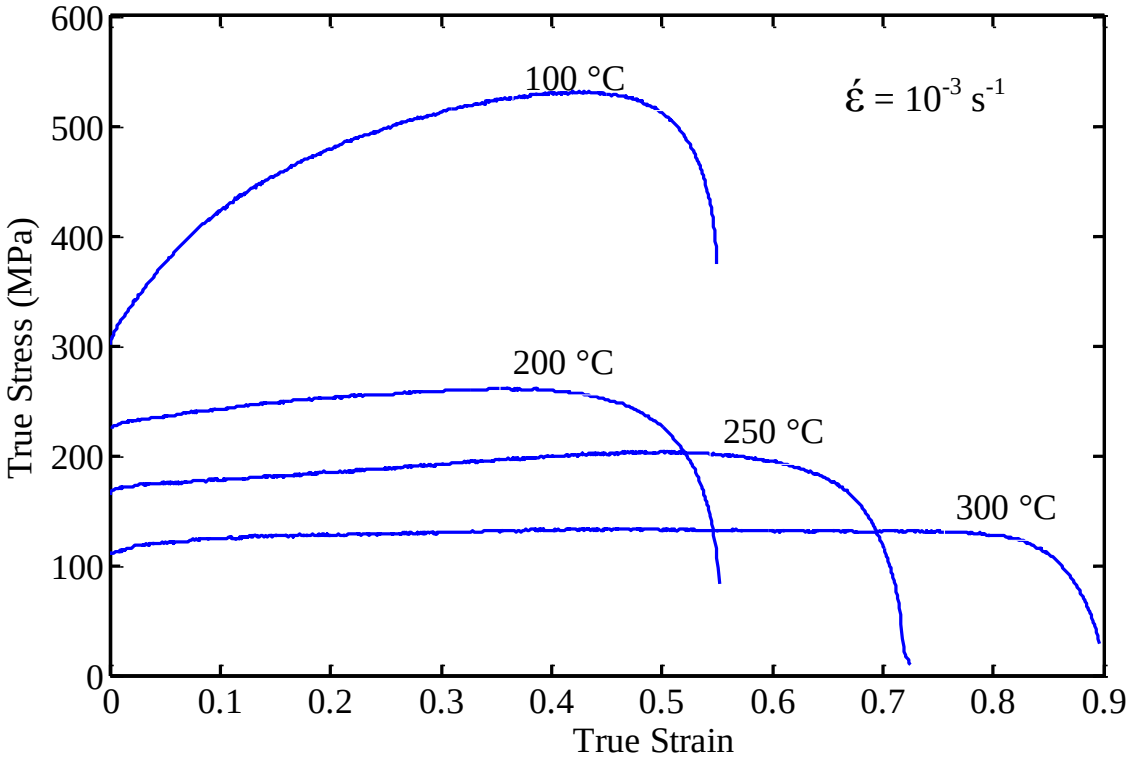

Figure 5.12: Specimens tested at a constant true-strain rate of 10^{-3} s^{-1} and the temperatures of room temperature (22°C), 100°C, 200°C, 250°C and 300°C are shown for TD parallel to the LTD. Stress decreases with increasing temperature. Strain at rupture increases as temperature increases between 200 and 300°C.

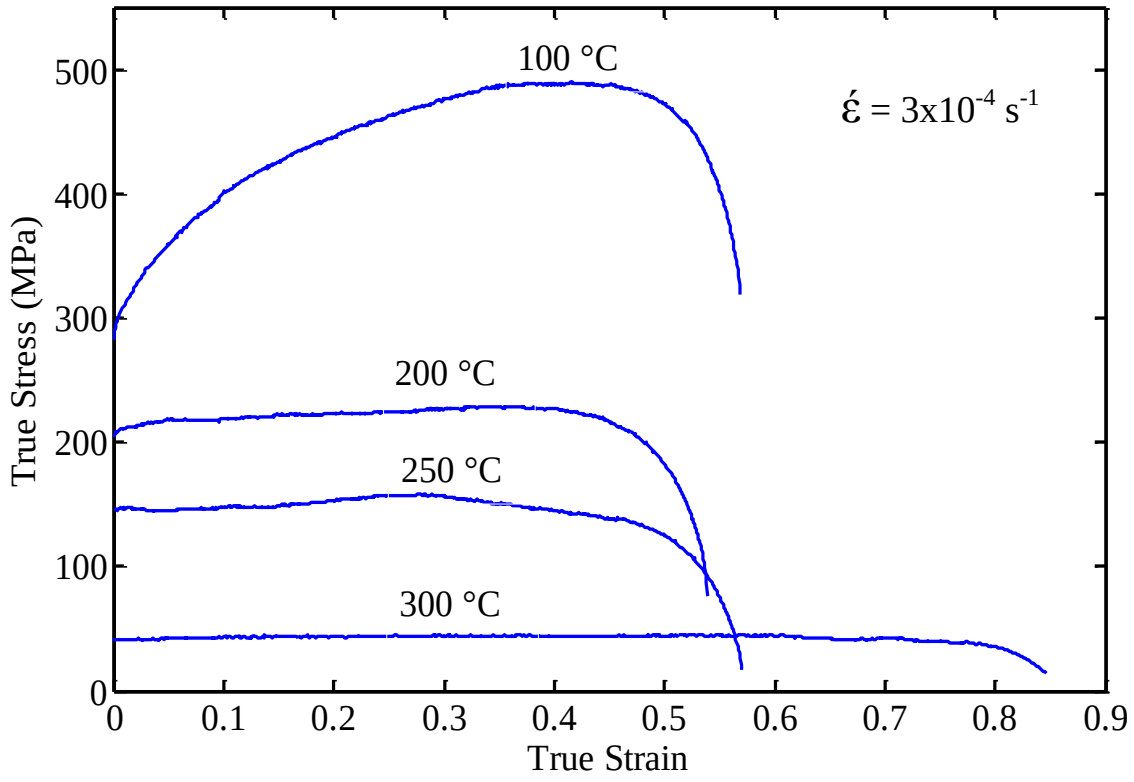

Figure 5.13: Specimens tested at a constant true-strain rate of 3x10^{-4} s^{-1} and the temperatures of room temperature (22°C), 100°C, 200°C, 250°C and 300°C are shown for TD parallel to the LTD. Stress decreases with increasing temperature. Strain at rupture increases as temperature increases between 200 and 300°C.

Table 5.1 provides tensile elongation and reduction in area at different temperatures and strain rates. These data were measured from all the specimens tested at different temperatures and strain rates. The greatest elongation, 106 % was obtained from a specimen tested at 10^{-3} s^{-1} and 300°C. Reduction in area increases with increasing

tensile elongation. This shows that, with increasing temperature and decreasing strain rate, better ductility can be obtained.

Table 5.1: Tensile elongation and reduction in area for specimens tested with the TD parallel to the LTD.

Temperature (°C)	***Strain Rate (s^{-1})***	***Starting Length (mm)***	***Final Displacement (to rupture) (mm)***	***Elongation (%)***	***Reduction in Area (%)***
300	10^{-1}	25	24.396	97.6	83.4
	10^{-2}	25	24.567	98.3	88.1
	10^{-3}	25	26.454	105.8	88.7
250	10^{-1}	25	19.386	77.5	74.1
	10^{-2}	25	23.566	94.3	80.5
	10^{-3}	25	24.862	99.5	82.9
200	10^{-1}	25	16.644	66.5	73.4
	10^{-2}	25	20.951	83.8	75.3
	10^{-3}	25	20.218	80.8	76.9
100	10^{-1}	25	11.702	46.8	50.6
	10^{-2}	25	17.458	69.3	59.3
	10^{-3}	25	19.944	79.8	67.2
RT (22)	10^{-1}	25	7.521	30.0	16.1
	10^{-2}	25	7.851	31.4	17.8

Figures 5.14 – 15 compare data from specimens oriented with the TD parallel to LTD, RD and 45^0 at 300 °C and 250 °C for a fixed-strain rate of 10^{-2} s^{-1}. Fixed-strain tests were conducted to ε=0.2 at 300 °C, 250 °C, 200 °C, 100 °C for TD parallel to LTD, RD and 45^0 orientations. As can be seen from Figures 5.14 – 15, flow stress increases with increasing true strain for all specimens. It is assumed that this behavior is a type of strain hardening [1]. Flow stress of specimens with the TD parallel to RD is approximately 25% higher than the other orientations at both temperatures.

Table 5.2 shows the R values obtained from fixed-strain (ε=0.2) tests for different specimen orientations. Since necking did not occur in fixed-strain tests, more reliable R-values were obtained than for tests to rupture. As can be seen from the data, at constant strain rate, the R-value increases toward unity with increasing temperature. This suggests that higher temperatures are less susceptible to plastic anisotropy from crystallographic texture than are lower temperatures [4].

It is seen from Table 5.2 that R-values do not dependent significantly on strain rate at 350 °C and 450 °C. This is because, for 350 °C and 450 °C, DC creep alone likely controls the deformation [1]. However, at 300 °C the R-values depend more strongly on strain rate. For the same orientation, the R-value decreases with decreasing strain rate.

At all temperatures, for a constant strain rate, the R-values for the TD parallel to RD are higher than for the TD parallel to LTD and 45^0. This is because the RD is harder than the LTD and 45^0 in-plane directions [1, 4].

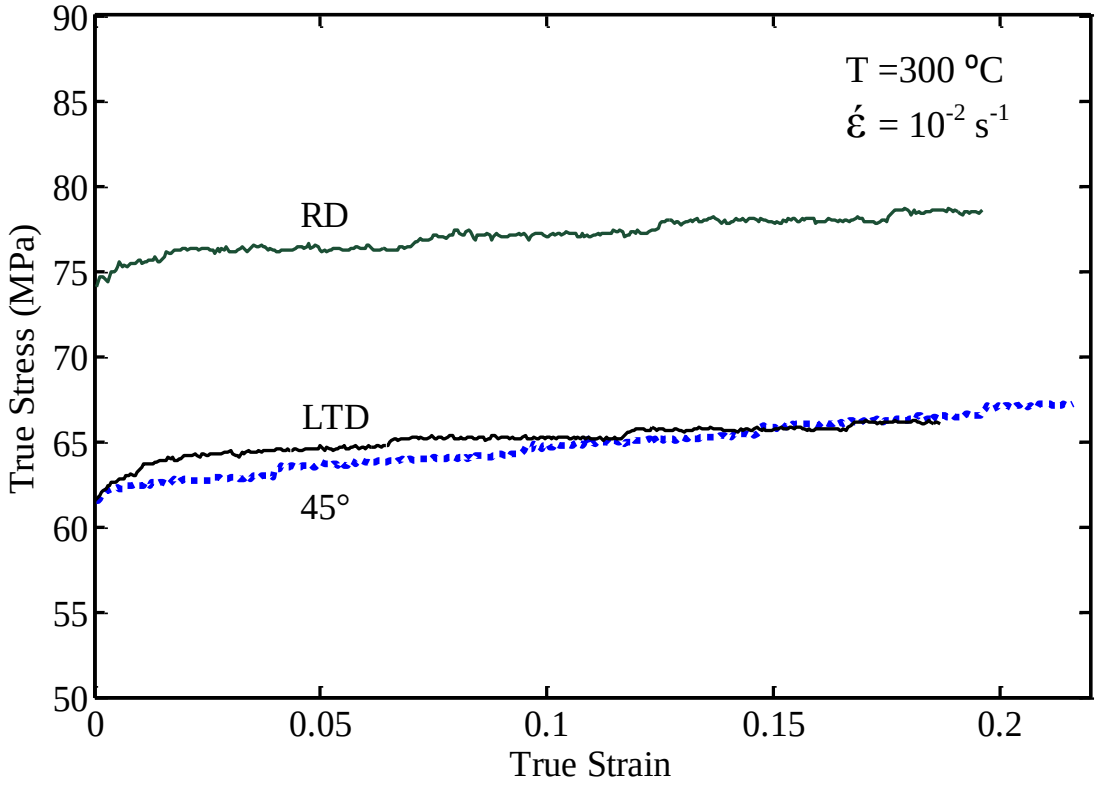

Figure 5.14: Fixed-strain test results are shown for specimens tested with the TD parallel to RD, LTD and 45^0 at 300°C and 10^{-2} s^{-1} The RD is the hard in-plane direction for deformation at 300°C.

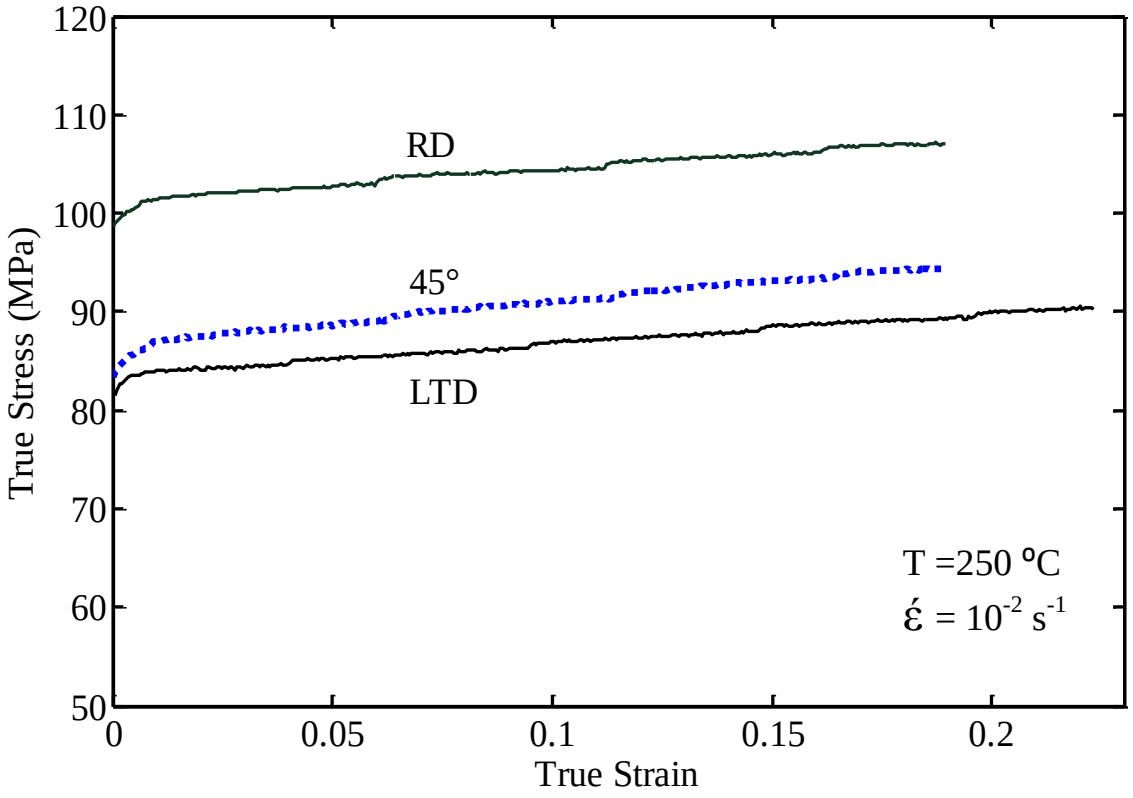

Figure 5.15: Fixed-strain test results are shown for specimens tested with the TD parallel to RD, LTD and 45^0 at 250°C and 10^{-2} s^{-1} The RD is the hard in-plane direction for deformation at 250°C.

Table 5.2: R-values obtained from fixed-strain tension tests, for the TD parallel to the LTD, RD and 45^0 at temperatures of 450 °C, 350°C, 300 °C, 250 °C, 200 °C and 100°C and strain rates of $3x10^{-4}$ s^{-1}, 10^{-3} s^{-1}, 10^{-2} s^{-1} and 10^{-1} s^{-1}. Data at 450°C and 350°C were taken from Ref. 1.

Temp (°C)	*Strain Rate (s-1)*	*Specimen Designation*	*True Strain*	*R Value*
450	**10^{-3}**	RD	0.24 ± 0.01	0.88 ± 0.07
		45°	0.27 ± 0.01	0.88 ± 0.05
		LTD	0.23 ± 0.01	0.81 ± 0.05
	10^{-2}	RD	0.14 ± 0.01	0.90 ± 0.04
		45°	0.15 ± 0.01	0.86 ± 0.05
		LTD	0.14 ± 0.01	0.81 ± 0.04
350	**10^{-3}**	RD	0.29 ± 0.01	0.82 ± 0.05
		45°	0.33 ± 0.01	0.79 ± 0.09
		LTD	0.31 ± 0.01	0.67 ± 0.06
	10^{-1}	RD	0.17 ± 0.01	0.79 ± 0.08
		45°	0.15 ± 0.01	0.78 ± 0.06
		LTD	0.18 ± 0.01	0.63 ± 0.07
300	**$3x10^{-4}$**	RD	0.18 ± 0.01	0.57 ± 0.09
		45°	0.18 ± 0.01	0.54 ± 0.07
		LTD	0.18 ± 0.01	0.51 ± 0.07
	10^{-2}	RD	0.19 ± 0.01	0.73 ± 0.06
		45°	0.21 ± 0.01	0.71 ± 0.08
		LTD	0.18 ± 0.01	0.62 ± 0.07
250	**10^{-2}**	RD	0.19 ± 0.01	0.74 ± 0.06
		45°	0.22 ± 0.01	0.69 ± 0.06
		LTD	0.18 ± 0.01	0.56 ± 0.06
200	**10^{-2}**	RD	0.21 ± 0.01	0.65 ± 0.09
		45°	0.22 ± 0.01	0.61 ± 0.05
		LTD	0.21 ± 0.01	0.59 ± 0.06
100	**10^{-2}**	LTD	0.22 ± 0.01	0.57 ± 0.08

5.2. BIAXIAL BULGE DATA

Figure 5.16 shows the experimental results of gas-pressure bulge tests that were conducted at 300 °C. Tests were conducted at The University of Texas at Austin laboratory. Figure 3.2 shows the bulge test machine system used for the tests. Tests were conducted at five different pressures from 2.06 MPa (300 psi) to 2.62 MPa (380 psi). For each pressure, dome height is plotted against the forming time. As seen in Fig 5.2.1, forming time decreases with increasing pressure. Depending on the pressure, forming time ranges from approximately 1000 sec to 4000 sec.

Biaxial bulge test results were used to validate the material constitutive models by comparing the FEM predictions with experimental results. These comparisons will be shown in chapter 7.

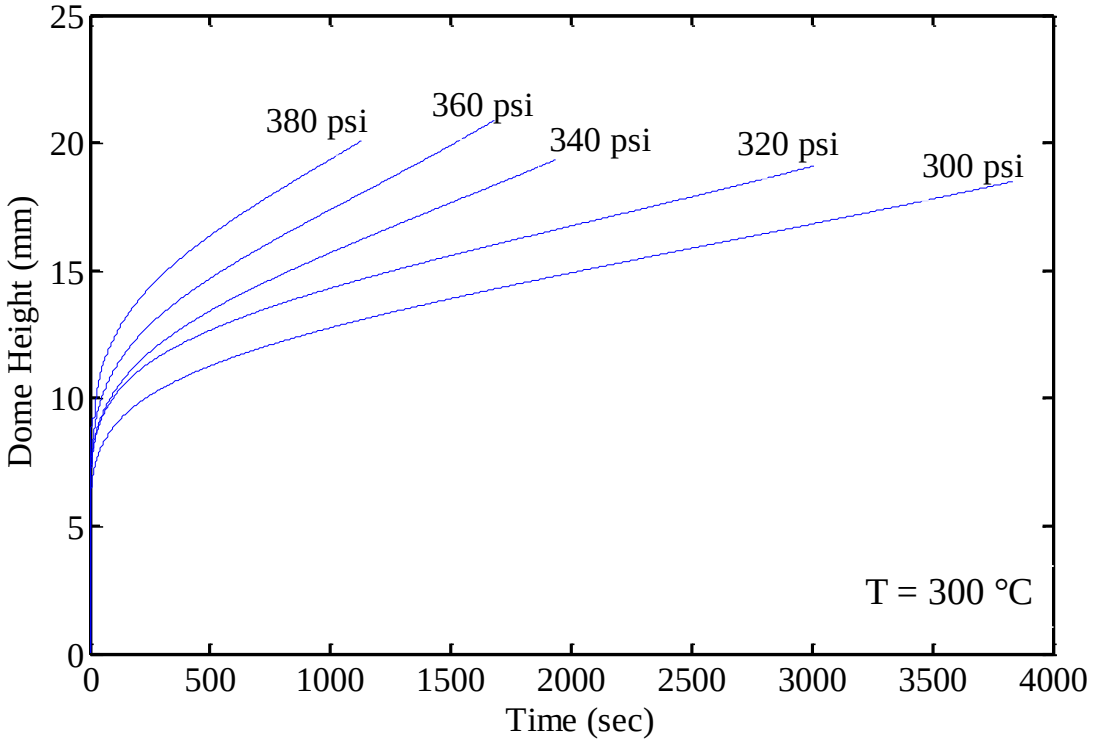

Figure 5.16: Dome height is plotted against forming time at 300°C for gas pressures of 300 psi (2.06 MPa), 320 psi (2.20 MPa), 340 psi (2.34 MPa), 360 psi (2.48 MPa) and 380 psi (2.62 MPa). Forming time decreases with increasing pressure.

REFERENCES

1. A.R. Antoniswamy, "The Construction and Use of Physics-Based Plasticity Models and Forming-Limit Diagrams to Predict Elevated Temperature Forming of Three Magnesium Alloy Sheet Materials," PhD Thesis, University of Texas at Austin, (2013).
2. S.L. Robinson, O.D. Sherby, Mechanical Behavior of Polycrystalline Tungsten at Elevated Temperature, Acta Metall., 17(2), 1969, pp. 109-125
3. O.A. Ruano, A.K. Miller, O.D. Sherby, The Influence of Pipe Diffusion on the Creep of Fine-grained Materials, Mater. Sci. Eng., 51(1), 1981, pp. 9-16.

4. K. Hantzsche, J. Wendt, K.U. Kainer, J. Bohlen, D. Letzig, Mg Sheet: The Effect of Process Parameters and Alloy Composition on Texture and Mechanical Properties, JOM, 61(8), 2009, p 38-42.

Chapter 6: Material Constitutive Models Development

6.1. Analysis of Tensile Data

Figure 6.1 shows the calculated stress exponent, n, value for temperatures from 22 °C to 450 °C. In this figure the true strain rate is plotted against the true stress on logarithmic scales. For each temperature above room temperature, tests were conducted for at least three strain rates. For room temperature, tests were conducted at two strain rates. For the temperatures of 450 °C and 350 °C, the data were taken from Antoniswamy [1]. On this plot, the slope of each line gives the stress exponent, *n,* value at that temperature. As seen in Figure 6.1, flow stress increases with decreasing temperature. The *n* values vary from 86.5 at low temperature to 4.8 at high temperatures. The *n* values are important to determine the deformation mechanisms active in the material at the different temperatures. When calculated *n* values were compared with the literature, it was determined that dislocation-climb (DC) creep controlled by lattice self-diffusion is the main deformation mechanism at 350 and 450 °C [1]. For 250 and 300 °C, it was concluded that DC creep controlled by pipe diffusion is the main deformation mechanism [2, 3]. From 22 °C to 200 °C, dislocation slip is thought to be the deformation mechanism that controls plastic deformation of Mg alloys [1, 4, 5]. The inverse of the *n* value is the strain-rate-sensitivity, *m,* value. For ZEK100 alloy sheet, the *m* values range from 0.208 to 0.011 for the temperatures from 450 °C to 22 °C.

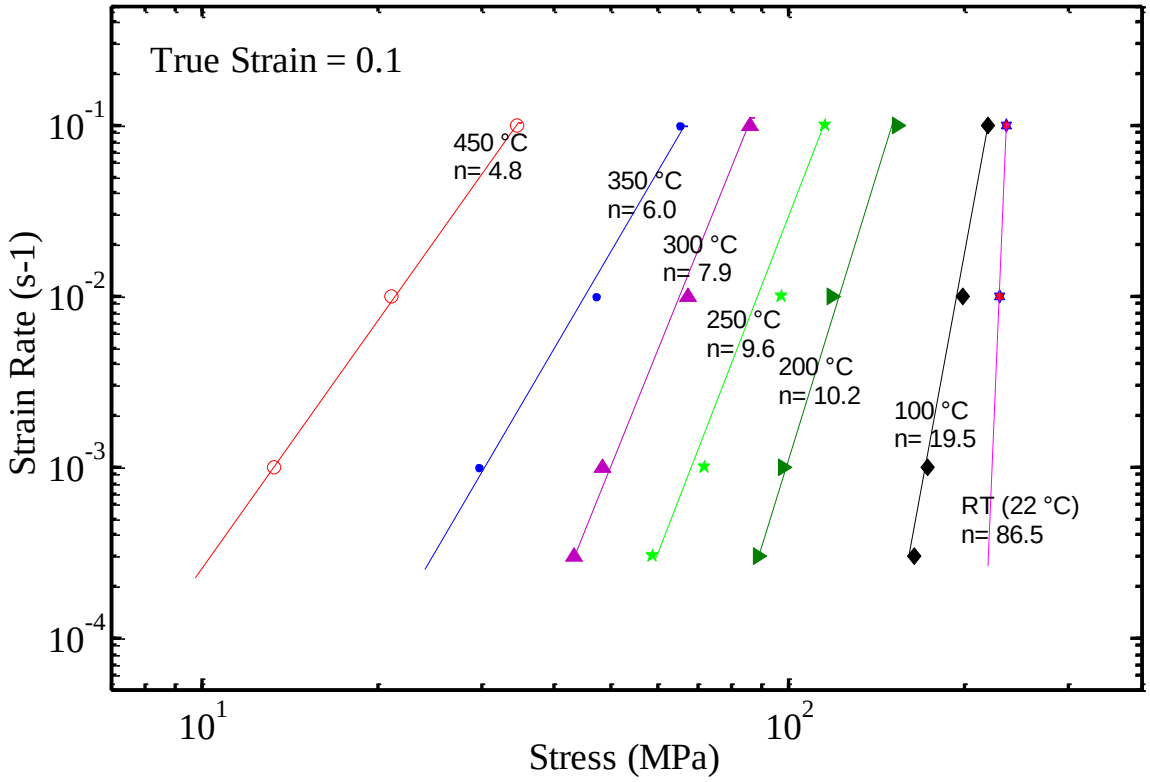

Figure 6.1: True strain rate is plotted as function of true stress (MPa) on logarithmic scales at temperatures from 450 °C to 22 °C (RT). The data are for 0.1 true-strain. The slope of the data at each temperature is the stress exponent, n. Data at 450 °C and 350 °C were taken from Ref. 1

Figure 6.2 shows the change of *n* value with changing strain rate at a constant temperature of 300 °C. At slow strain rates the *n* value is close to 6. With increasing strain rate, the *n* value increases to 9. The increasing *n* value with strain rate suggests the increasing importance of pipe diffusion to dislocation creep, as was pointed out by Antoniswamy [1]. The data shown in Figure 6.2 were taken at two different strains, 0.1 and 0.2. The flow stresses at Ɛ=0.2 are slightly stronger than those at Ɛ=0.1, and this is because of moderate strain hardening. This is the same effect identified by Antoniswamy at higher temperatures.

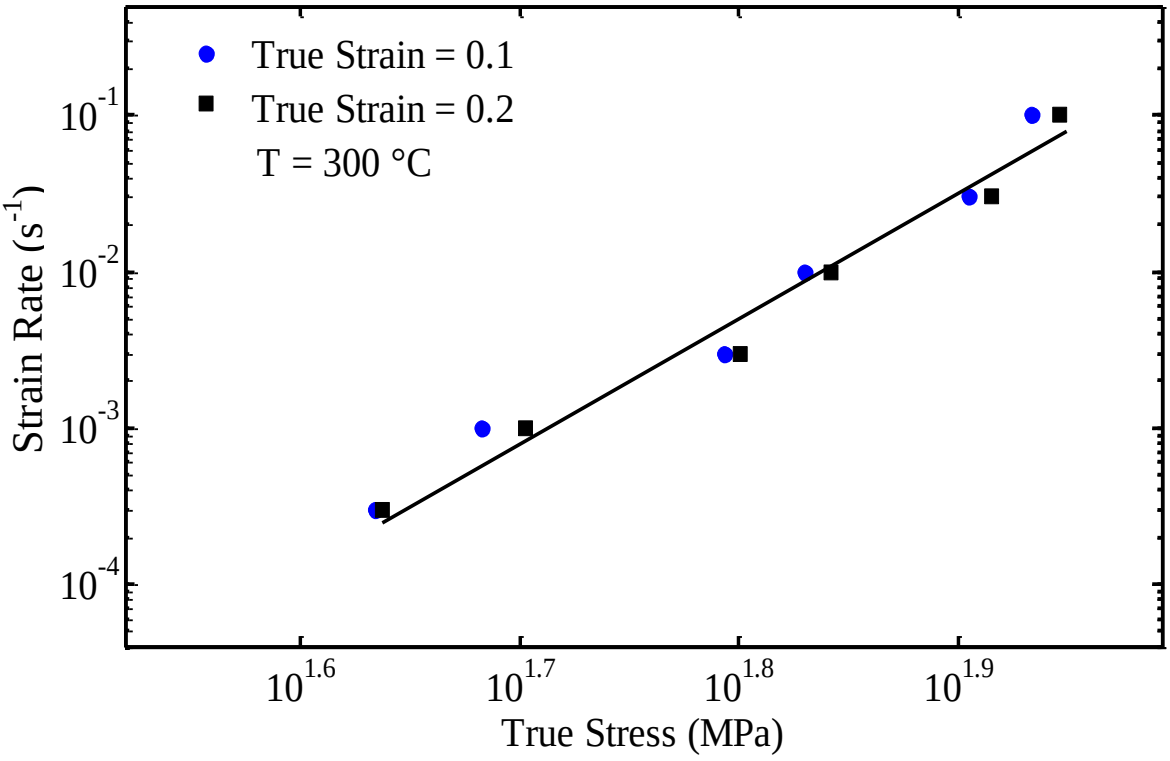

Figure 6.2: True strain rate is plotted as a function of true stress (σ) on logarithmic scales at 300 °C for two different true strains (ε), 0.1 and 0.2.

Approximately steady state creep is observed for the temperatures above 0.75 T_m in wrought Mg ZEK100 [1]. Likely because ZEK100 contains rare-earth elements, some strain hardening was observed even at high temperatures [1, 3]. The Zener-Hollomon parameter, *Z*, considers the effects of both temperature and strain rate during steady state creep. The effects of the strain rate and temperature on *Z* are demonstrated in equations 1 and 2 [9].

$$Z = \dot{\varepsilon} \times \exp(Q/\mathrm{RT}) \quad (1)$$

$$Z = A \times (\sinh[\alpha \times \left(\frac{\sigma}{E}\right)])^n \quad (2)$$

where *Z* is the Zener-Hollomon parameter, $\dot{\varepsilon}$ is the strain rate (s^{-1}); *n* is the stress exponent; α and *A* are material constants that depend on the deformation mechanisms; σ

is the flow stress (MPa) of the material; Q is the activation energy of deformation (J/mol); R is the universal gas constant (8.314 J/mol K); and T is the absolute temperature (K). Equation 1 is the definition of the Zener-Hollomon parameter [9]. Equation 2 demonstrates the *sinh* relationship proposed by Garofalo to fit data into the regime of power-law-breakdown [18].

The displacement *versus* time data were obtained from uniaxial tension tests. These data were used to calculate stress-strain values for each test. The calculated stress-strain data were corrected by using the machine stiffness [1]. For this correction, elastic modulus, *E(T),* was used for each temperature. Equation 4 shows the calculation of elastic modulus for each temperature. The slope of the elastic loading region was corrected by using *E(T).* In Equation 3, T is the temperature in K and *E(T)* is the elastic modulus in MPa [1].

$$E(T)=48666-8.587\times T-0.0194\times T^2 \quad (3)$$

The Z parameter was calculated at temperatures from 22 °C to 300 °C for the test data. The Z parameters at 350 °C and 450 °C were also calculated by using the data of Antoniswamy [1]. Figure 6.3 shows the calculated Z parameters *versus* true stress normalized by the elastic modulus on logarithmic scales for all temperatures from 450 °C to 22°C. For these calculations, the activation energy for creep was taken as 112 kJ/mol [8]. Since there is no single equation that can easily fit the data at all temperatures, the data of Figure 6.3 were separated into three categories: data from 450 °C to 22 °C, 450 °C to 100 °C and 450 °C to 200 °C. For each category, the most accurate available equation was fitted to data [9]. The results were optimized by using the least-square fitting method. Fitted equations are shown in Figure 6.3 for each. The Z parameter ranges

between approximately 10^5 s^{-1} and 10^{19} s^{-1}. The Z parameter increases with decreasing temperature and increasing strain rate. Figure 6.3 also shows that Z increases with increasing σ/E. For Z parameters from 10^5 s^{-1} to 10^{12} s^{-1}, the stress exponent increases from n= 4.8± 0.3 to n=10.2± 0.9. Figure 6.3 shows that power-law breakdown occurs at approximately $Z=10^{12}$ s^{-1} [1].

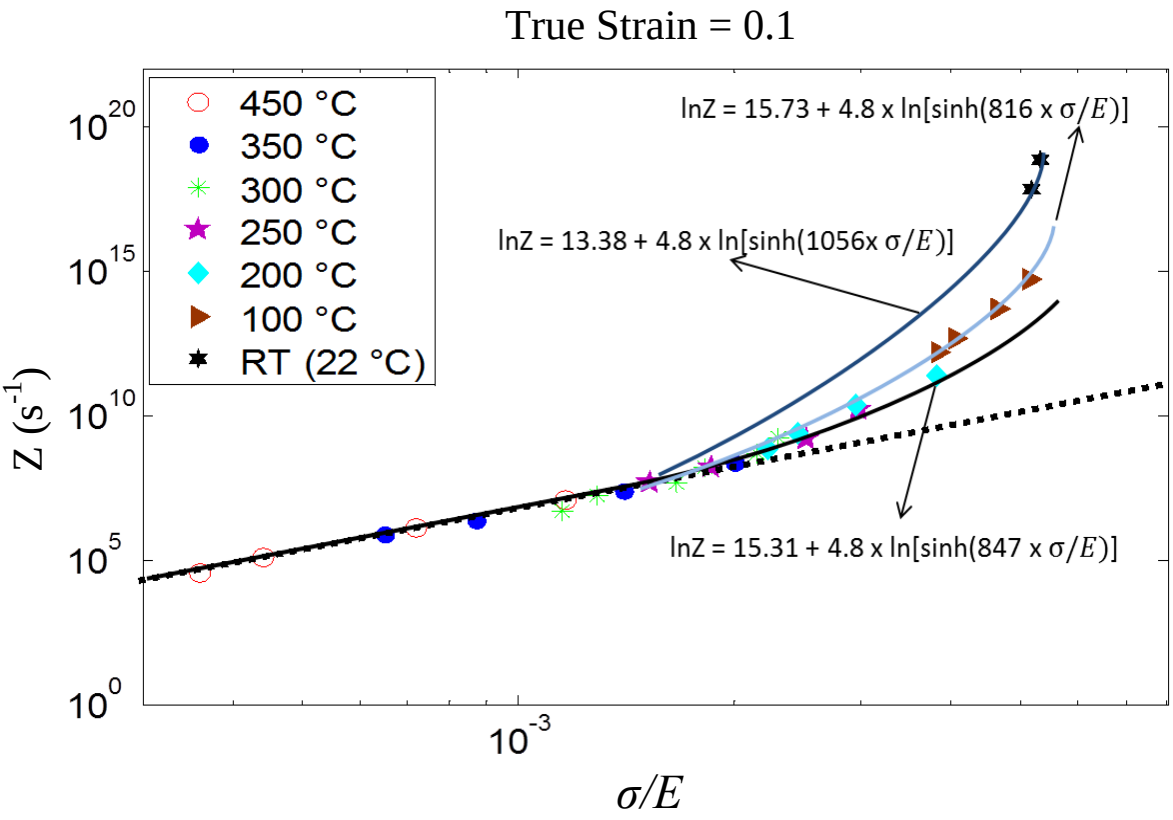

Figure 6.3: The Zener-Holloman parameter is shown as a function of σ/E (modulus compensated stress). Activation energy, Q, was taken as 112 kJ/mol for calculations of Z. Data were calculated for a true strain of ε = 0.1. Data for 450 °C and 350 °C were taken from Ref. 1.

Because of power-law breakdown, the equation for power-law creep cannot be accurately used at temperatures lower than 200 °C [1]. Thus, activation energies were

only calculated for the temperatures higher than 200 °C, $T \geq 200$ °C. The activation energy, Q, values were calculated using the method shown in Figure 6.4. For each temperature, the experimental data were plotted as true-strain rate *versus* true-stress normalized by temperature-dependent elastic modulus at a constant true strain of $\mathcal{E} = 0.1$ on dual logarithmic scales. Then, a line was fit to these data for each temperature. For each temperature, error bounds were calculated using the root-mean-square (RMS) method. These error bounds are shown as dashed lines in Fig 6.1.4. For each region, constant σ/E values were chosen. Then, strain rates at each temperature were read from the plot at each constant σ/E value. These data were used to create a new plot of true-strain rates as a function of $1/T$ at constant σ/E values. On this plot, each temperature was represented by a curve. The slopes of these curves are equal to $-Q/R$, where R is the universal gas constant. Thus, Q values were calculated at each σ/E value. The uncertainties of these slopes were calculated using the Monte Carlo Method [1]. Table 6.1 shows the calculated Q values for different ranges of temperature. Figure 6.5 shows the Q values plotted against T/T_m, where T_m is the melting temperature of the Mg ZEK100 alloy sheet (650 °C).

Table 6.1: Activation energies are provided as a function of temperature. The errors shown were calculated from a Monte-Carlo simulation using Mathematica™ software.

Temperature Range (°C)	Activation energy ± error (kJ/mol)
450 - 300	128 ± 10.9
350 - 250	129 ± 24.5
300 - 200	109 ± 11.4

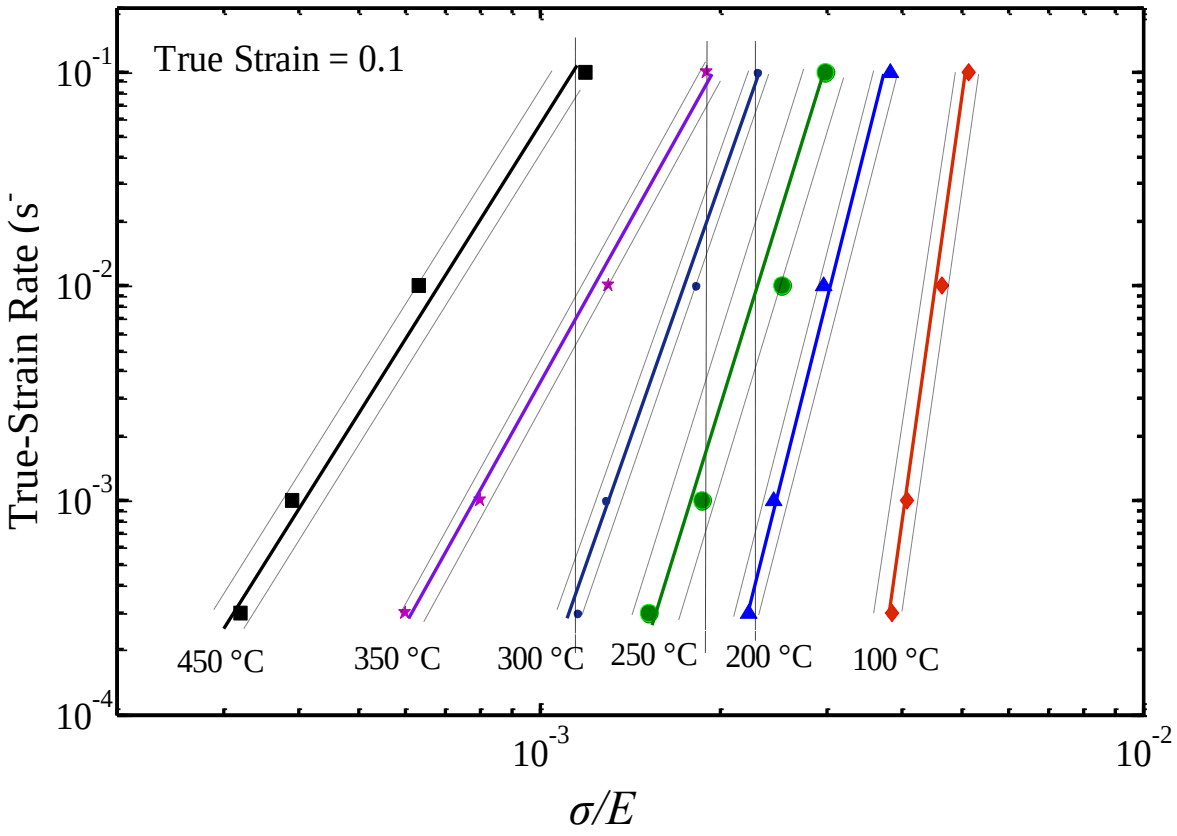

Figure 6.4: Data are shown for Mg ZEK100 at temperatures from 450 °C to 100 °C and a constant true strain value of 0.1. True-strain rate is plotted against the true stress compensated by the temperature dependent elastic modulus, σ/E, on logarithmic scales. The solid lines show the best fit to the data at each temperature and the dashed lines show the calculated error bounds. The vertical dashed lines show the chosen σ/E values. Data at 450 °C and 350 °C were obtained from Ref. 1.

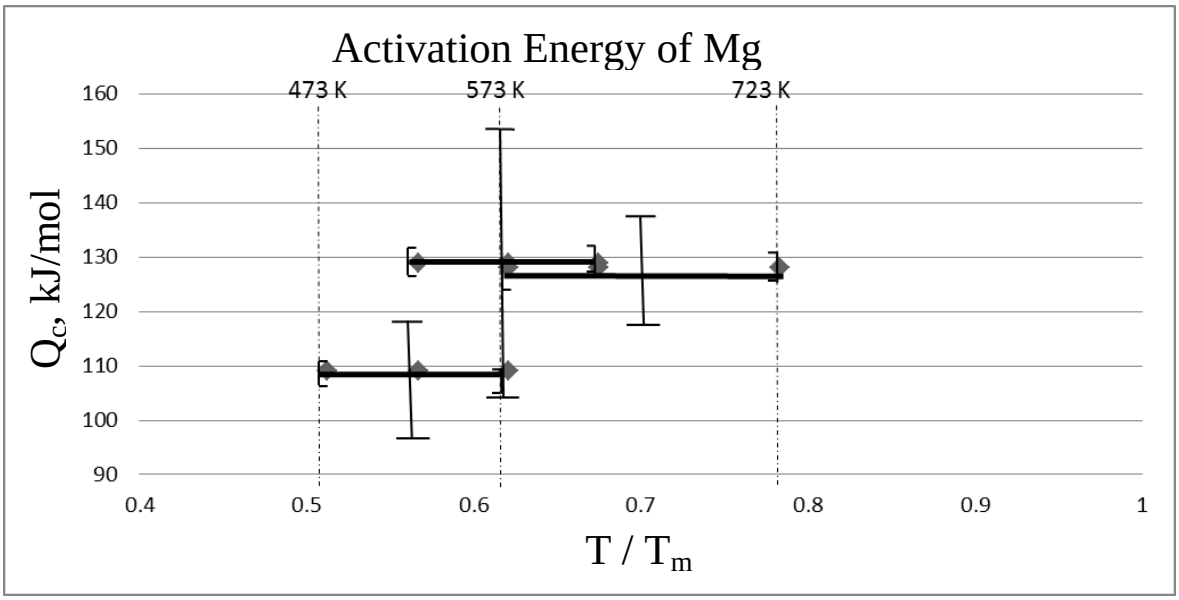

Figure 6.5: Activation energies, Q (kJ/mol) are shown against temperature normalized by melting temperature (T/T_m) for Mg ZEK100. Error bars were calculated using a Monte Carlo simulation.

The activation energy calculated for 200 °C to 300 °C is 109±11.4 kJ/mol, for 250 °C to 350 °C is 129±24.5 kJ/mol and for 300 °C to 450 °C is 128±10.9 kJ/mol. Activation energies for diffusion in pure Mg are reported in the literature for several temperatures [1, 8, 9]. Values from Frost and Ashby are shown in Table 6.2 [8]. The Q value of 109 kJ/mol measured for 200 °C to 300 °C is close to the 92 kJ/mol reported by Frost and Ashby for dislocation pipe diffusion. This suggests that DC creep is rate controlled by dislocation pipe diffusion in this range of low temperatures. Likewise, for the 250 °C to 350 °C and the 300 °C to 450 °C temperature ranges, the calculated Q values are close to 135 kJ/mol, which is consistent with DC creep controlled by lattice self-diffusion [1, 8]. The Q values suggest the active deformation mechanisms in each temperature range.

Table 6.2: Activation energies for diffusion in pure Mg. Data were taken from Frost and Ashby, Ref. 8.

Activation Energy (kJ/mol)	Diffusion Mechanism
92	Dislocation Pipe Diffusion
135	Lattice Self Diffusion

6.2. MATERIAL MODELS

To describe the creep response, it was helpful to create material constitutive models [1, 15]. Axial tension test results, stress-strain data and the calculated R-values were used to construct material constitutive models. In this study, for Mg ZEK100, material models were constructed for temperatures of 300 °C and 250 °C. These models were used in finite-element-method (FEM) simulations. Results of these FEM simulations were compared with the experimental biaxial bulge test results. Thus, the material constitutive models were validated against independent data.

In literature, most of the material constitutive models are constructed for only a single creep mechanism [10-14]. However, it was previously shown that deformation is controlled by dislocation-creep (DC) and grain-boundary-sliding (GBS) creep together for the AZ31Mg alloy at high temperature [1, 14, 15]. Recently, Carpenter et al. [15] constructed an accurate model for these Mg alloys at 450 °C. In this new model, DC and GBS creep were considered together. The effects of grain growth and normal anisotropy were also taken into account in their model. Then, Antoniswamy [1] modified that model for Mg ZEK100 alloy sheet. In the modified model, DC creep controlled by lattice self-

diffusion and/or pipe diffusion was also considered. In this study, the model created by Carpenter et. al. [15] and modified by Antoniswamy [1] was used. The model was previously used and validated by Antoniswamy [1] for Mg ZEK100 at the temperatures of 350 °C and 450 °C. However, it was not previously applied to temperatures of 250 °C and 300 °C.

During DC creep in the ZEK100 alloy sheet true flow stress increases with increasing true strain at 300 °C and 250 °C. R values at 300 °C and 250 °C also change with changing strain rate. These effects are because of anisotropy differences between the creep mechanisms [1]. Effects of normal anisotropy in Mg AZ31 were taken into account by calculating R_{eff}, as shown in Equation 4 [15]. In this equation, f_{DC} is the fraction of DC creep strain as a proportion of the total true strain; as shown in Equation 5 [1, 15].

$$R_{eff} = \frac{R_{GBS}(1+R_{DC})(1-f_{DC}) + R_{DC}(1+R_{GBS})f_{DC}}{(1+R_{DC})(1-f_{DC}) + (1+R_{GBS})f_{DC}} \quad (4)$$

$$f_{DC} = \frac{\varepsilon_{DC}}{\varepsilon_{GBS} + \varepsilon_{DC}} \quad (5)$$

where ε_{GBS} is the true strain from GBS creep and ε_{DC} is the true strain from DC creep. For temperatures from 250 ^{0}C to 300 ^{0}C, DC creep is controlled primarily by pipe diffusion, $\varepsilon DC(p)$. Since GBS creep is not active in ZEK100 at these temperatures, f_{DC} was assumed to be one for these conditions [1]. The effects of plastic anisotropy on plastic flow were calculated using the Hill equation,

$$\sigma_H = \sqrt{F\sigma_{22}{}^2 + G\sigma_{11}{}^2 + H(\sigma_{11} - \sigma_{22})^2 + 2N\sigma_{12}{}^2} \quad (6)$$

This calculated stress was used in FEM simulations to define the plastic anisotropy. In this equation F, G, H and N are the coefficients of the planar anisotropy defined in Equation 7, 8, 9 and 10 [1].

$$F = \frac{1}{2}\left(\frac{1}{R22^2} + \frac{1}{R33^2} - \frac{1}{R11^2}\right) \quad (7)$$

$$G = \frac{1}{2}\left(\frac{1}{R33^2} + \frac{1}{R11^2} - \frac{1}{R22^2}\right) \quad (8)$$

$$H = \frac{1}{2}\left(\frac{1}{R11^2} + \frac{1}{R22^2} - \frac{1}{R33^2}\right) \quad (9)$$

$$N = \frac{3}{2R12^2} \quad (10)$$

where $R_{12,}$ $R_{11,}$ R_{22} and R_{33} were calculated by using the *R*-values from the uniaxial tension test results [1]. Since ZEK100 exhibits planar anisotropy, a single *R*-value cannot be used, as was previously the case for Mg AZ31 sheet alloys [1]. The $R_{12,}$ $R_{11,}$ R_{22} and R_{33} values need to be calculated separately. The R_{11} value is approximately equal to one from the experimental data. The $R_{12,}$ R_{22} and R_{33} values can be calculated by using Equations 11, 12 and 13 [1].

$$R_{12} = \sqrt{\frac{3(R_{RD}+1)R_{LTD}}{(R_{RD}+R_{LTD})(2R_{45}+1)}} \quad (11)$$

$$R_{22} = \sqrt{\frac{R_{LTD}(1+R_{RD})}{R_{RD}(1+R_{LTD})}} \quad (12)$$

$$R_{33} = \sqrt{\frac{R_{LTD}(1+R_{RD})}{(R_{RD}+R_{LTD})}} \quad (13)$$

where the R_{RD}, R_{LTD} and R_{45} values were previously calculated in chapter 5.

For material constitutive models, Equation 14 was used as the general equation for strain rate. However, for the ZEK100 alloy sheet, DC creep controlled by pipe diffusion, $\varepsilon_{DC(p)}$, is the only active deformation mechanism at 250 ^{0}C and 300 ^{0}C. The reason for this was explained in Chapter 6.1. Because of that, ε_{GBS} and $\varepsilon_{DC(l)}$ were assumed to be zero. Thus Equation 14 can be rewritten as Equation 15.

$$\dot{\varepsilon} = \dot{\varepsilon}_{GBS} + \dot{\varepsilon}_{DC(l)} + \dot{\varepsilon}_{DC(p)} \quad (14)$$

$$\dot{\varepsilon} \cong \dot{\varepsilon}_{DC(p)} \quad (15)$$

Equation 15 was used in simulations. This equation leads to Equation 16 for ZEK100 alloy sheet, where A is the pre-exponential factor, n is the stress exponent for DC creep controlled by pipe diffusion and $\dot{\varepsilon}$ is the true-strain rate. [1].

$$\dot{\varepsilon} = A_{DC(p)}\sigma(\varepsilon)^{n_{DC(p)}} \quad (16)$$

Calculated fit parameters at 300 ^{0}C and 250 ^{0}C are shown in Table 6.3 for *DC(p)*. The error bounds of $A_{DC(p)}$ and $n_{DC(p)}$ were calculated by using the RMS method. Thus, the best fit parameters were calculated.

Table 6.3: Fit parameters for ZEK100 alloy sheet at 250 °C and 300 °C.

Fit Parameters *A, n*	250 °C	300 °C
$A_{DC(p)}$	$\exp(-37.45-4.30\varepsilon+8.53\varepsilon^2-8.99\varepsilon^3)$	$\exp(-37.58-5.02\varepsilon+17.93\varepsilon^2-30.24\varepsilon^3)$
$n_{DC(p)}$	8.8	7.9

Material constitutive models were constructed for ZEK100 at temperatures of 300 °C and 250 °C. To validate these models, experimental results of biaxial bulge tests were used. FEM simulations were calculated with the Abaqus/Standard™ FEM software. Results of these FEM simulations were compared against the experimental results. More information will be provided on these comparisons in Chapter 7. Material models were validated at a temperature of 300 °C.

REFERENCES

1. A.R. Antoniswamy, "The Construction and Use of Physics-Based Plasticity Models and Forming-Limit Diagrams to Predict Elevated Temperature Forming of Three Magnesium Alloy Sheet Materials," PhD Thesis, University of Texas at Austin, (2013).
2. S.L. Robinson, O.D. Sherby, Mechanical Behavior of Polycrystalline Tungsten at Elevated Temperature, Acta Metall., 17(2), 1969, pp. 109-125
3. O.A. Ruano, A.K. Miller, O.D. Sherby, The Influence of Pipe Diffusion on the Creep of Fine-grained Materials, Mater. Sci. Eng., 51(1), 1981, pp. 9-16.
4. S. R. Agnew, O. Duygulu, "Plastic Anisotropy and the Role of Non-basal Slip in Magnesium Alloy AZ31B," International Journal of Plasticity, 21 (2005), pp. 1161-1193.
5. J. Koike, R. Ohyama, T. Kobayashi, M. Suzuki and K. Maruyama, "Grain-Boundary Sliding in AZ31 Magnesium Alloys at Room Temperature to 523K," Materials Transactions, 44 (2003), pp. 445-451.
6. W. Köster, "Die Temperaturabhängigkeit des ElisatizitätsmodulsreinerMetalle," Zeitschriet für Metallkunde, 39 (1948), pp. 1–9.
7. O.A. Ruano, A.K. Miller, O.D. Sherby, The Influence of Pipe Diffusion on the Creep of Fine-grained Materials, Mater. Sci. Eng., 51(1), 1981, pp. 9-16.
8. H.J. Frost, M.F. Ashby," Deformation Mechanism Map", Pergamon Press, Elmsford, NY, (1982), p 44.
9. Y. Jia, "Hot deformation behavior of spray-deposited Al–Zn–Mg–Cu alloy", Materials and Design, (2014), p 79-85.

10. H.-K. Kim, W.-J. Kim, Creep Behavior of AZ31 Magnesium Alloy at Low Temperature Range between 423 K and 473 K, J. Mater. Sci., 2007, 42(15) , pp. 6171-6176.
11. I.A. Maksoud, H. Ahmed, J. Rödel, Investigation of the Effect of Strain Rate and Temperature on the Deformability and Microstructure Evolution of AZ31 Magnesium Alloy, Mater. Sci. Eng. A, 2009, 504(1), pp. 40-48.
12. S. Spigarelli, M. El Mehtedi, Creep as an Extension of Hot Working: A Unified Approach to High Temperature Deformation of AZ31 Alloy, Mater. Sci. Eng. A, 2010, 527(21), pp. 5708-5714.
13. C. Bruni, L. Donati, M. El Mehtedi, M. Simoncini, Constitutive Models for AZ31 Magnesium Alloys, Key Eng. Mater., 2008, 367, pp. 87-94.
14. K.E. Tello, A.P. Gerlich, P.F. Mendez, Constants for Hot Deformation Constitutive

    Models for Recent Experimental Data, Sci. Technol. Weld. Joining, 2010, 15(3), pp. 260-266.
15. A.J. Carpenter, Physics-Based Material Constitutive Models for the Simulation of High-Temperature Forming of Magnesium Alloy AZ31, PhD Thesis, University of Texas at Austin, (2012).
16. P.A. Sherek, Simulation and Experimental Investigation of Hot Gas-Pressure Forming for Light-Alloy Sheet Material, Thesis, Mechanical Engineering, The University of Texas at Austin, 2009.
17. P.A. Sherek, A.J. Carpenter, L.G. Hector, Jr., P.E. Krajewski, J.T. Carter, J. Lasceski, E.M. Taleff, The Effects of Strain and Stress State in Hot Forming of Mg AZ31 Sheet, Magnesium Technology, Wiley, 2012, pp. 301-306.

18. O. D. Sherby, P. M. Burke, Mechanical Behavior of Crystalline Solid at Elevated Temperature, Acta Metall., 1968, pp. 325-386

Chapter 7: Finite-Element-Method Simulations

7.1. Simulation Methods

FEM simulations were used to validate the material constitutive models constructed for Mg ZEK100 alloy sheet at 300 °C and 250 °C. To run the FEM simulations, commercial Abaqus™ software was used. Material constitutive models were defined for FEM simulations by using the FORTRAN 77 language [1]. The two-term material models were defined by using the uniaxial tests results [2]. A CREEP subroutine was used to define the material models in FEM simulations. For each temperature, one CREEP file was created. To define how the material behaves at that temperature. An example CREEP.F file in the FORTRAN 77 language is provided in Appendix 7.1.A.

Mg ZEK100 exhibits planar anisotropy at 300 °C and 250 °C [3]. Because of that, a 2-dimensional (2D) axisymmetric mesh is not appropriate for simulations at 300 °C and 250 °C [3]. In this study, a 3D mesh was used for simulations at 300 °C and 250 °C. The 3D mesh was developed by Sherek [4], and it was used before by Antoniswamy [3] for ZEK100 at 450 °C and 350 °C. For the FEM simulations, the specimen diameter was taken as 90 mm and the specimen thickness was taken as 1.56 mm. These values are the same as the biaxial bulge tests specimens. One example of the 3D mesh is shown in Figure 7.1. In this figure, Mg ZEK100 alloy sheet was formed in the FEM simulation.

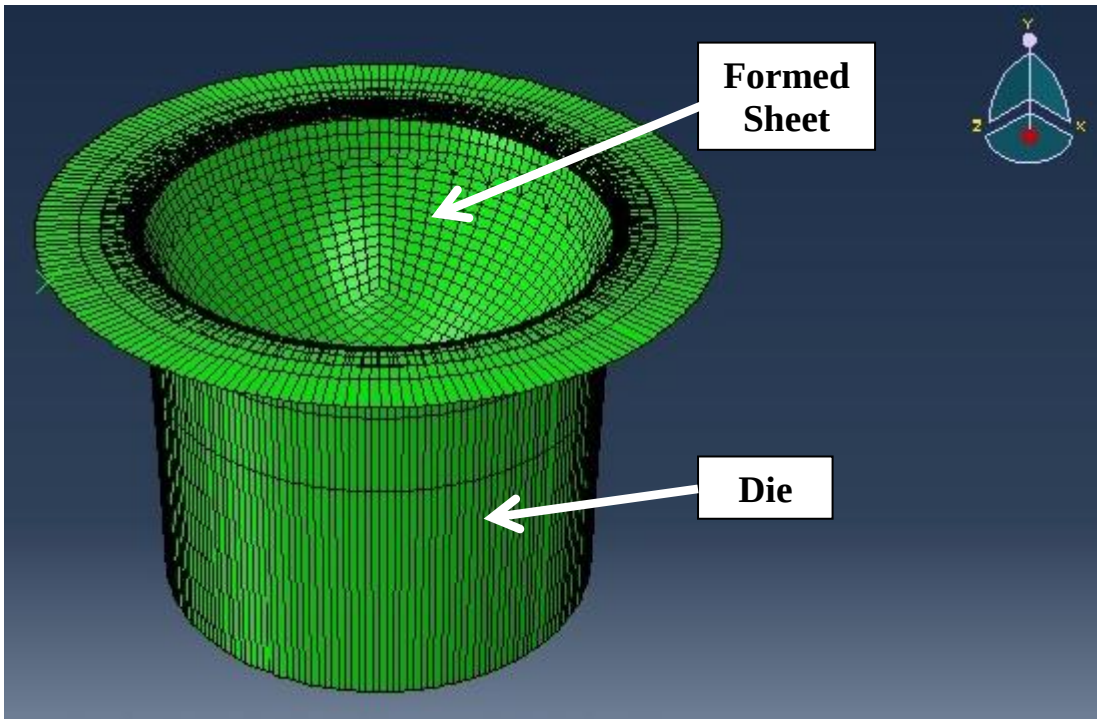

Figure 7.1: FEM simulation of the biaxial bulge test is shown using a 3D mesh for the ZEK100 alloy sheet.

FEM simulations were conducted at temperatures of 250 °C and 300 °C and pressures of 2.06 MPa (300 psi), 2.20 MPa (320 psi), 2.34 MPa (340 psi), 2.48 MPa (360 psi) and 2.62 MPa (380 psi). Simulation times were chosen to be the same as the experimental tests. Thus, results of the FEM simulations and experimental tests could be compared on the same scales. From the FEM simulations, dome height *versus* time and pole thickness *versus* time predictions were obtained. Dome height *versus* time was obtained from simulations and compared to experimental results from biaxial bulge tests. Thus, the validity of the material constitutive models was proven for 300 °C. Since Mg ZEK100 exhibits the same deformation mechanisms at 250 °C as at 300 °C, simulation results at 250 °C were also expected to be good, although bulge test data were not available at 250 °C. Simulation predictions were also compared with the results of

Antoniswamy [3] at 450 °C and 350 °C. The results of these comparisons are shown in Section 7.2.

7.2. COMPARISON BETWEEN FEM SIMULATIONS AND EXPERIMENTS

FEM simulations were conducted at temperatures of 250 °C, 300 °C, 350 °C and 450 °C. For 300 °C, simulations were conducted at pressures of 2.06 MPa (300 psi), 2.20 MPa (320 psi), 2.34MPa (340 psi), 2.48 MPa (340 psi) and 2.62 MPa (360 psi). Figures 7.2 – 7.6 show comparisons of the predictions from FEM simulations against the experimental biaxial bulge test data. The validity of the material model was proven by these comparisons. In these figures, dome height *versus* time predictions from FEM simulations and data from experiments are compared. The error between the simulation predictions and the experimental data for dome height was calculated using the Root-Mean-Square (RMS) method. The formulization of the RMS method is shown in Equation 1, where X_{RMS} is the RMS error (mm), n is the total number of comparisons, X_{exp} is dome height of experiment and X_{sim} is the dome height of FEM simulation [3].

$$x_{RMS} = \sqrt{\frac{1}{n}\sum_{i=1}^{n}\left(x_{\exp} - x_{sim}\right)^2} \qquad (1)$$

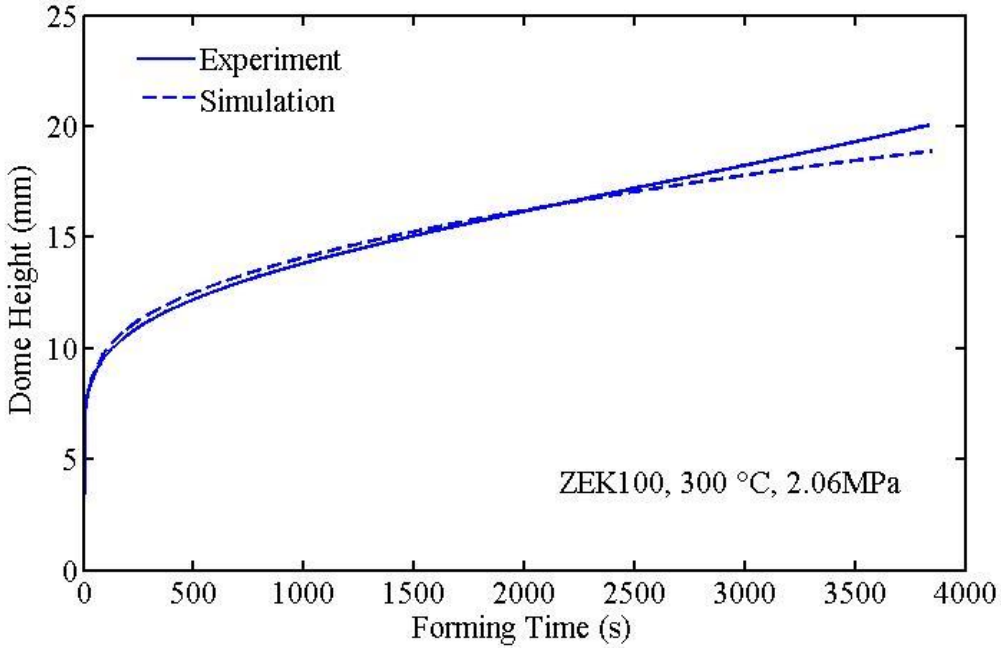

Figure 7.2: Dome height *versus* forming time is shown for the temperature of 300 °C at a constant pressure of 2.06 MPa (300 psi) for Mg ZEK100 alloy sheet.

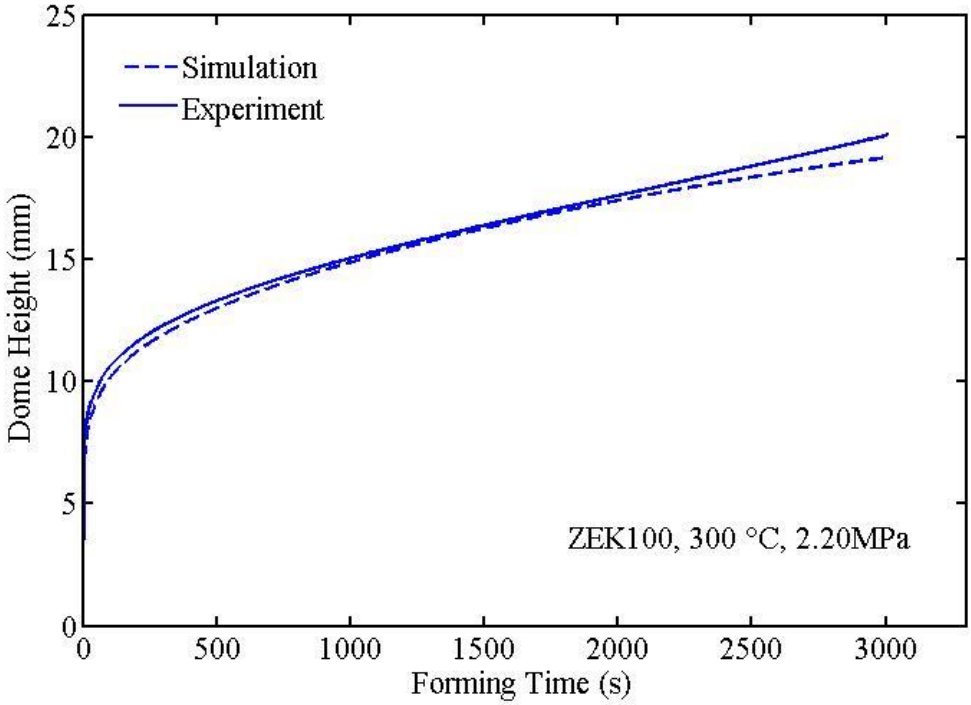

Figure 7.3: Dome height *versus* forming time is shown for the temperature of 300 °C at a constant pressure of 2.20 MPa (320 psi) for Mg ZEK100 alloy sheet.

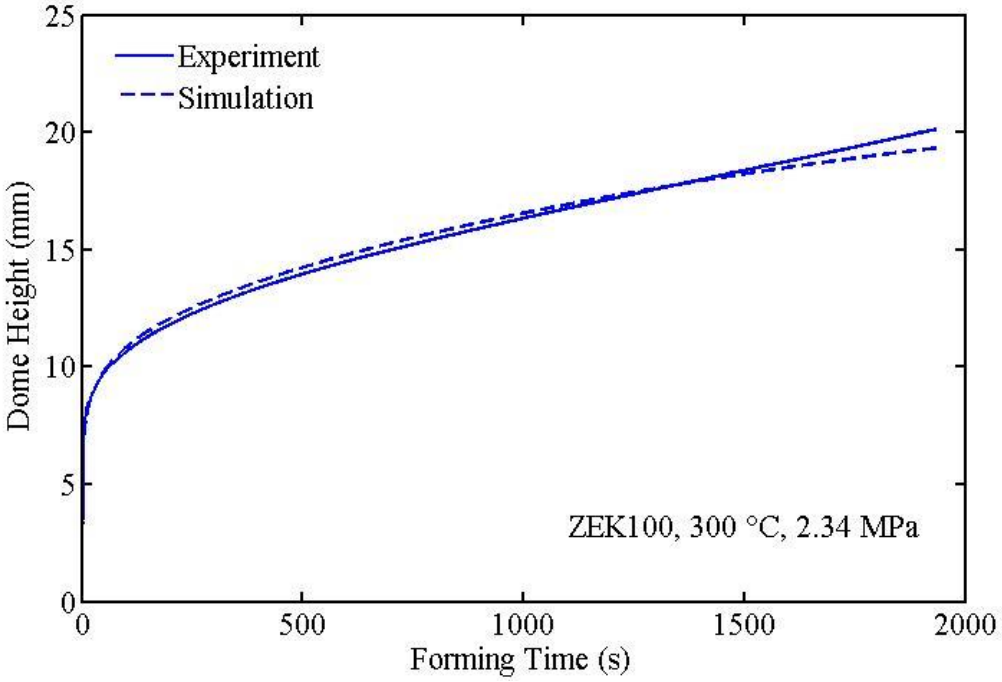

Figure 7.4: Dome height *versus* forming time is shown for the temperature of 300 °C at a constant pressure of 2.34 MPa (340 psi) for Mg ZEK100 alloy sheet.

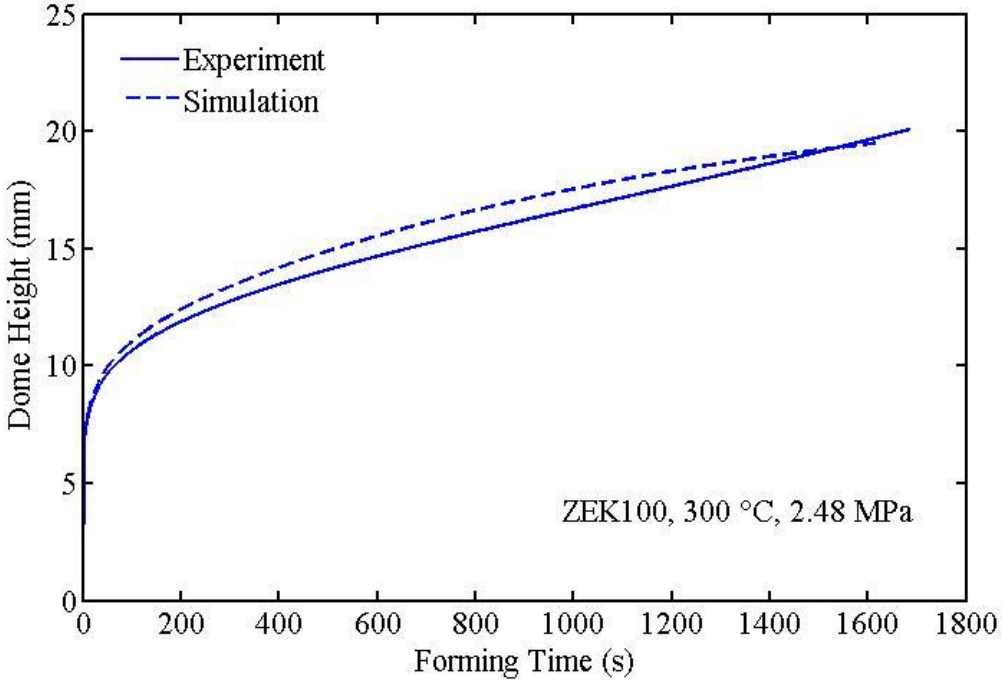

Figure 7.5: Dome height *versus* forming time is shown for the temperature of 300 °C at a constant pressure of 2.48 MPa (360 psi) for Mg ZEK100 alloy sheet.

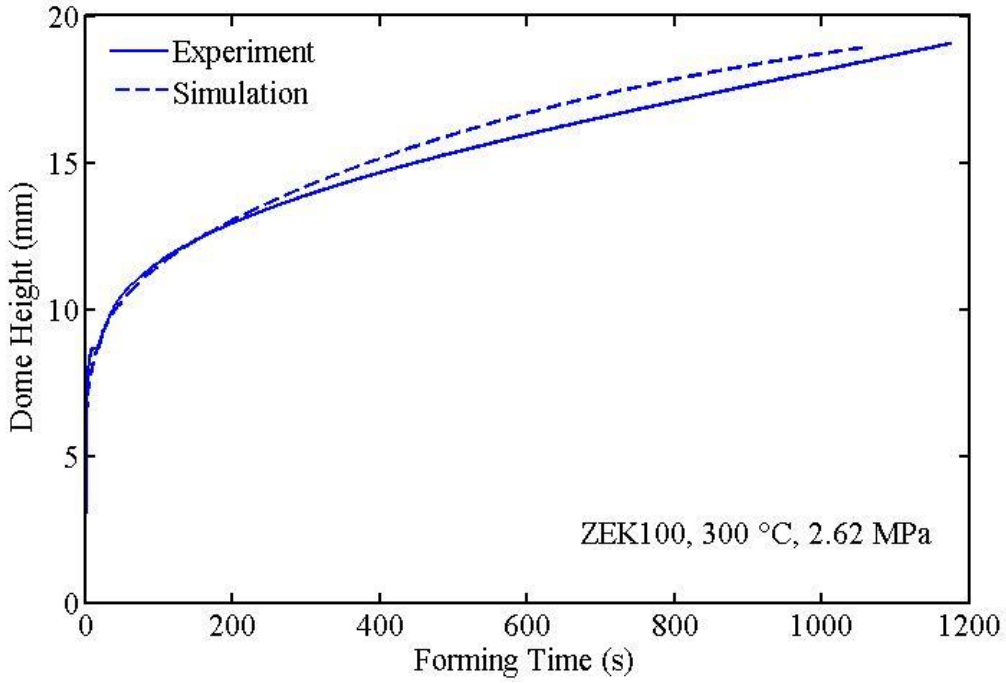

Figure 7.6: Dome height *versus* forming time is shown for the temperature of 300 °C at a constant pressure of 2.62 MPa (380 psi) for Mg ZEK100 alloy sheet.

For 300 °C, the effect of pressure on the forming time was investigated by comparing dome height *versus* time for all pressures. Figure 7.7 shows this comparison. Forming time decreases with increasing pressure at equal dome height.

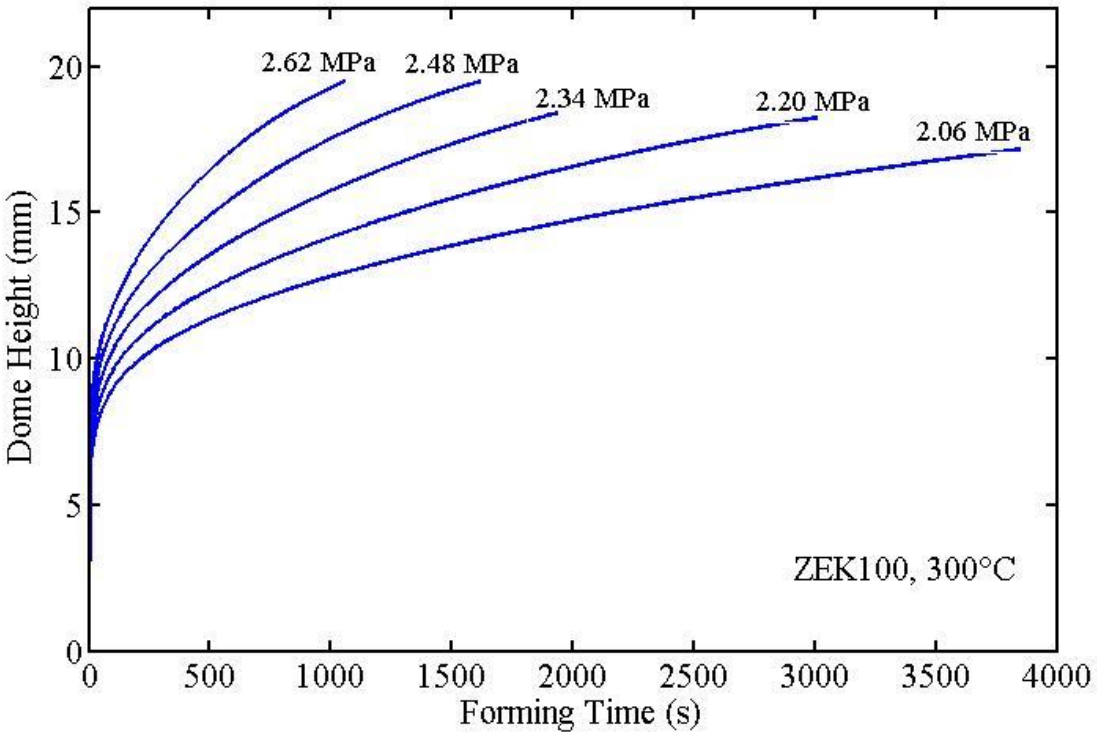

Figure 7.7: The effect of pressure on the forming time at equal dome height is shown at a constant temperature of 300 °C for Mg ZEK100 alloy sheet using FEM simulation predictions.

For 250 °C, simulations were conducted for the pressures of 2.06 MPa (300 psi) and 2.62 MPa (380 psi). Figure 7.8 shows dome height *versus* forming time obtained from FEM simulations at 250 °C.

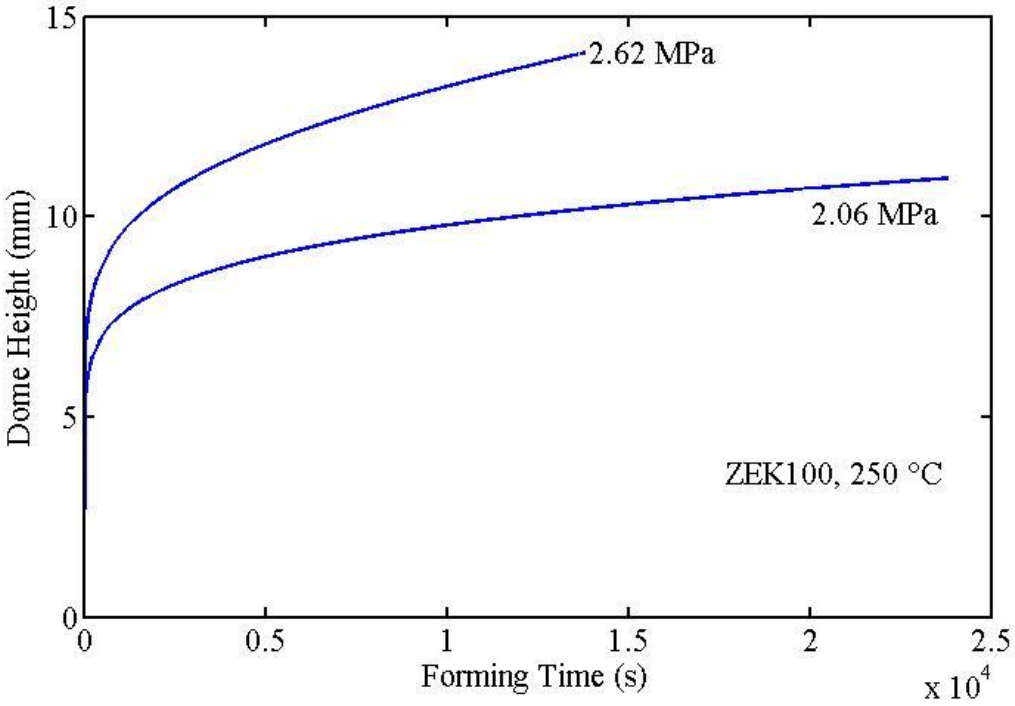

Figure 7.8: FEM simulation predictions of dome height *versus* forming time are shown for the temperature of 250 °C and the pressures of 2.06 MPa (300 psi) and 2.62 MPa (380 psi) for Mg ZEK100 alloy sheet.

FEM simulations were conducted for the temperatures of 350 °C and 450 °C at a constant pressure of 2.06 MPa (300 psi) by using information from Antoniswamy [3]. Dome height *versus* forming time obtained from simulations is shown on Figure 7.9.

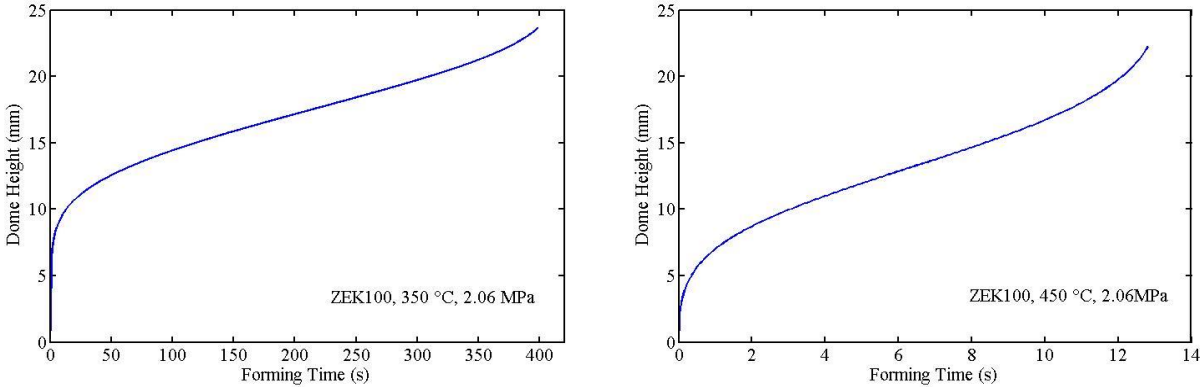

Figure 7.9: FEM simulation predictions of dome height *versus* forming time are shown for the temperatures of 350 °C and 450 °C at a constant pressure of 2.06 MPa (300 psi) for Mg ZEK100 alloy sheet. The data for 350 °C and 450 °C were taken from Ref. 3.

Pole thickness *versus* time was also examined for temperatures from 250 °C to 450 °C at a constant pressure of 2.06 MPa (300 psi). Figure 7.10 shows a comparison of pole thickness *versus* forming time while the dome height increases from 0 mm to 10 mm. The final pole thickness at a dome height equal to 10 mm occurs at the end of each simulation, and the change of pole thickness during forming is shown. Pole thickness at a 10 mm dome height decreases slightly with decreasing temperature from 450 °C to 250 °C. This shows the temperature effect on the pole thickness. The temperature effect on the forming time is examined in Figure 7.11.

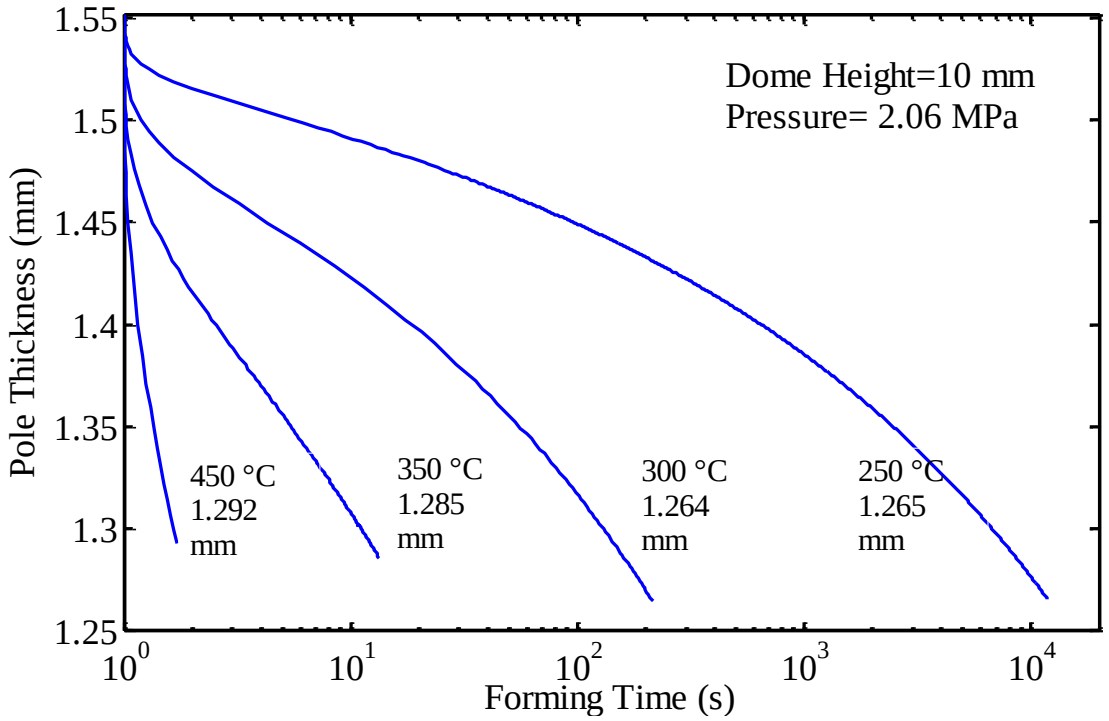

Figure 7.10: FEM simulation predictions of pole thickness *versus* forming time are shown for temperatures of 250 °C, 300 °C, 350 °C and 450 °C at a constant pressure of 2.06 MPa for Mg ZEK100 alloy sheet. The end of each simulation occurs at a dome height of 10 mm. Pole thickness at a 10 mm dome height decreases slightly with decreasing temperature from 450 °C to 250 °C.

Pole thickness *versus* forming time was also examined at a constant temperature of 300 °C and pressures from 2.06 MPa (300 psi) to 2.62 MPa (380 psi). FEM simulation predictions of pole thickness at a 10 mm dome height and the total time to reach a 10 mm dome height are shown in Table 7.1 for each pressure from 2.06 MPa to 2.62 MPa at a constant temperature of 300 °C. In Figure 7.7, forming time decreases with increasing test pressure. Test pressure does not affect the pole thickness of the specimen at a given dome height for a constant temperature. Thus, it can be said that the pole thickness at a

given pole thickness is independent from the forming pressure but depends on forming temperature for the range of pressures considered.

Table 7.1: FEM simulation predictions for pole thickness at a 10 mm dome height and total forming time to reach a 10 mm dome height are shown at a constant temperature of 300 °C and pressures of 2.06 MPa (300 psi), 2.20 MPa (320 psi), 2.34MPa (340 psi), 2.48 MPa (360 psi) and 2.62 MPa (380 psi). Forming time decreases with increasing test pressure. However, final pole thickness at a 10 mm dome height does not change with changing test pressure.

Forming Pressure *(MPa)*	Total Time to Reach 10 mm Dome Height *(sec)*	Pole Thickness at 10 mm Dome Height *(mm)*
2.06	215.5	1.2646
2.20	131.5	1.2645
2.34	81.2	1.2642
2.48	52.8	1.2641
2.62	34.8	1.2645

The effect of temperature on forming time is shown in Figure 7.11. Total time to reach a 10 mm dome height is plotted for temperatures from 250 °C to 450 °C. The predictions at 350 °C and 450 °C were taken from Ref. 3. In this figure, experimental results are also shown for 300 °C and 350 °C. Forming time decreases with increasing forming temperature.

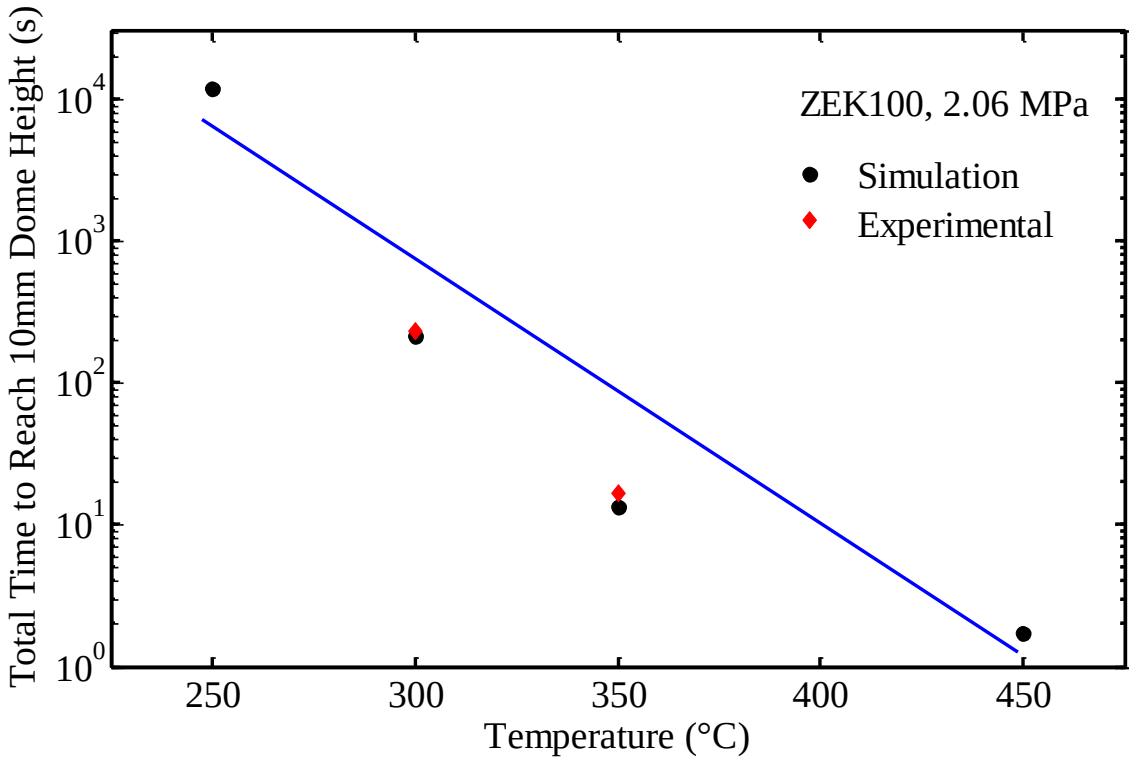

Figure 7.11: The effect of temperature on the forming time at constant pressure, 2.06 MPa (300 psi), is shown for FEM simulations of the Mg ZEK100 alloy sheet. The total time to reach a 10 mm dome height is plotted for temperatures from 250 °C to 450 °C. The data at 350 °C and 450 °C were taken from Ref. 3.

The material model was successfully validated at 300 °C by comparing simulation results with the experimental results of biaxial bulge tests. These comparisons are shown in Figures 7.2 – 7.6 for 300 °C and the pressures between 2.06 MPa (300 psi) and 2.62 MPa (380 psi). Simulations at 250 °C were also conducted by using a material model constructed in the same way as the material model of 300 °C. FEM simulations were conducted at 350 °C and 450 °C using information from Antoniswamy [3]. Results of these simulations were used to understand the temperature and pressure effects on pole

thickness and forming time. Forming time decreases with increasing test temperature. Pole thickness does not change with changing pressure for a given dome height while temperature is constant. However, while pressure is constant, pole thickness increases with increasing test temperature.

REFERENCES

1. J.W. Backus: FORTRAN 77, Armonk: IBM, 1978.
2. A.J. Carpenter, "Physics-Based Material Constitutive Models for the Simulation of High-Temperature Forming of Magnesium Alloy AZ31," PhD Thesis, University of Texas at Austin, (2012).
3. A.R. Antoniswamy, "The Construction and Use of Physics-Based Plasticity Models and Forming-Limit Diagrams to Predict Elevated Temperature Forming of Three Magnesium Alloy Sheet Materials," PhD Thesis, University of Texas at Austin, (2013).
4. P.A. Sherek, "Simulation and Experimental Investigation of Hot Gas-Pressure Forming for Light-Alloy Sheet Material, Thesis, Mechanical Engineering," Master Thesis, University of Texas at Austin, (2009).

Chapter 8: Conclusions and Future Work

This study shows that the material constitutive models constructed can be used to predict forming of Mg ZEK100 alloy sheet at temperatures of 250 °C and 300°C. It is expected that the material model is also accurate at 250 °C, but experimental data were not available to validate at this temperature. The Mg ZEK100 alloy sheet deforms by the same mechanisms at 250 °C and 300 °C. At the temperatures of 250 °C and 300 °C, the deformation mechanism is DC creep controlled by pipe diffusion. Thus, DC creep controlled by pipe diffusion was taken as the dominant deformation mechanism. Since the validity of material model was verified at 300 °C, it is assumed that the material model at 250 °C is valid as well.

To construct the material constitutive models, uniaxial tension test results, stress-strain data and R value calculations were used. To construct models for 250 °C and 300 °C, several steps were followed. First, deformation mechanisms were determined by using the stress exponent, n, values and the activation energies for creep, Q. It was observed that the active deformation mechanism for the Mg ZEK100 alloy sheet at 250 °C and 300 °C is DC creep controlled by pipe diffusion. From this observation, the material models were constructed. These models were successfully used in FEM simulations. Since Mg ZEK100 exhibits planar anisotropy, 3D FEM simulations were conducted by using the Abaqus™ software. The results of these simulations were used to validate the material models against independent experimental data. Furthermore, by using the results of FEM simulations several predictions were achieved related to the temperature and pressure effects on the pole thickness and the forming time. The pole thickness does not change with changing pressure for a given dome height at a constant temperature. However, at a constant pressure, increasing forming temperature increases

the pole thickness at a fixed dome height. Likewise, with increasing temperature forming time decreases.

The R-values decrease with increasing temperature from 22 °C to 300 °C for a constant strain rate. For all temperatures, the TD parallel to RD specimens exhibit higher R-values than TD parallel to LTD and 45^0 specimens at a constant strain. The TD parallel to RD is the hardest direction.

In this study, accurate material constitutive models were constructed for temperatures of 250 °C and 300°C. However these models do not give significant information about the deformation mechanisms at temperatures lower than 250 °C. Forming at lower temperatures provides significant advantages, such as energy savings, avoiding abnormal grain growth and easier part handling. These advantages are attractive to the automobile and aerospace industries. Therefore, it will be useful to construct material models for lower temperatures in the future. Furthermore, in this study grain size and pre-heating effects on forming were not investigated. It will be useful to investigate grain growth and pre-heating effects on forming in the future.

Appendix A Biaxial Bulge Test Specimens

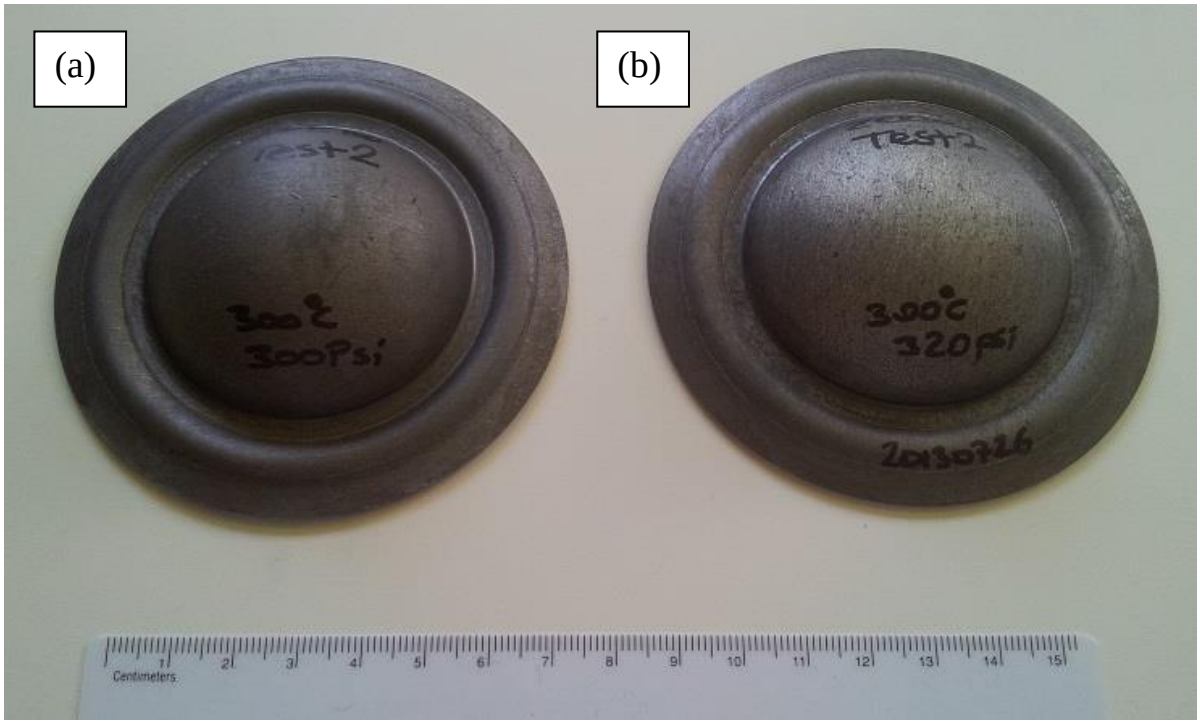

Figure A.1: Biaxial bulge tests were conducted at a temperature of 300 °C. Specimen (a) was tested at a pressure of 2.06 MPa (300 psi) and specimen (b) was tested at a pressure of 2.20 MPa (320 psi). Both of these tests were conducted until a dome height of 20 mm.

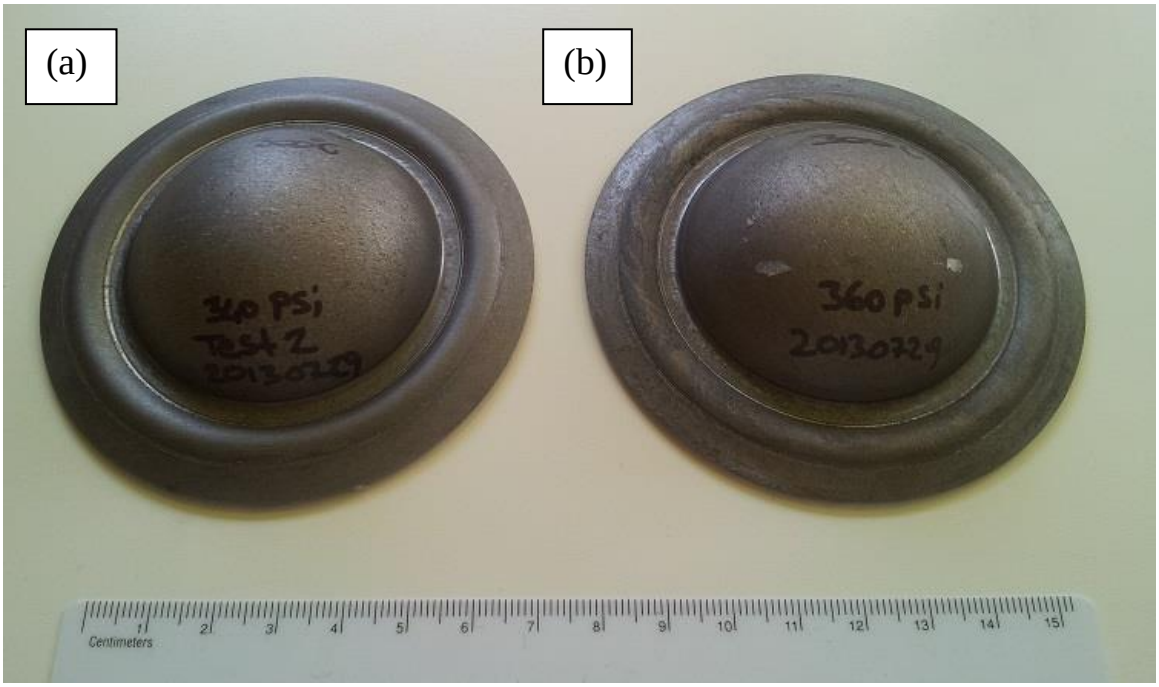

Figure A.2: Biaxial bulge tests were conducted at a temperature of 300 °C. Specimen (a) was tested at a pressure of 2.34 MPa (340 psi) and specimen (b) was tested at a pressure of 2.48 MPa (360 psi). Both of these tests were conducted until a dome height of 20 mm.

Figure A.3: A biaxial bulge test was conducted at a temperature of 300 °C and pressure of 2.62 MPa (380 psi). Testing was conducted until a dome height of 20 mm.

Appendix B Abaqus CREEP.F Files

EXAMPLE CREEP.F FILE FOR ZEK100 AT 250 °C

```
      C constitutive equation
      c     de/dt = A1(e)*sigma1^n1(e)+A2*sigma2^n2
      c           A1(e) = exp(-9.97333-12.5909e+17.8488e^2-11.0985e^3)
      c           n1(3) = 1.3325+0.667476tanh(4.6266e)

          SUBROUTINE
CREEP(DECRA,DESWA,STATEV,SERD,EC,ESW,P,QTILD,
         1
TEMP,DTEMP,PREDEF,DPRED,TIME,DTIME,CMNAME,LEXIMP,LEND,
        2 COORDS,NSTATV,NOEL,NPT,LAYER,KSPT,KSTEP,KINC)
         INCLUDE 'ABA_PARAM.INC'
         CHARACTER*80 CMNAME
         DIMENSION DECRA(5),DESWA(5),STATEV(*),PREDEF(*),DPRED(*),
        1 TIME(2),EC(2),ESW(2),COORDS(*)

      C-----------------------------------------------------------------+
      C-----------------------------------------------------------------+
      C--------------------------  DECLARATIONS  ------------------------*
      C-----------------------------------------------------------------+
          PARAMETER (dzero=1.D-20)
      C-----------------------------------------------------------------+
      C-----------------------------------------------------------------+
      C------------------  BEGINNING OF EXECUTABLE CODE  ------------------*
```

```
C-----------------------------------------------------------------------+
C-----------------------------------------------------------------------+
C
          A1 = exp(-44.1001-(9.01788*EC(2))
     1 +(27.3055*EC(2)**2)
     1 -(32.0014*EC(2)**3))
          dn1 = 8.8
C-----------------------------------------------------------------------+
C-------- Metal creep: Equivalent (uniaxial) deviatoric creep strain increment.
      DECRA(1)=(A1*QTILD**dn1)*DTIME
C-----------------------------------------------------------------------+
C-------- Metal creep: Derivative
C-------- DECRA(2): D(de^cr)/D(e^cr)
C-------- DECRA(5): D(de^cr)/D(q)

C Calculate the appropriate derivatives of the creep strain increment
      IF(LEXIMP.EQ.1) THEN
      DA1De = A1*(-9.01788+54.611*EC(2)-96.0042*EC(2)**2)
          DECRA(2)=(DA1De*QTILD**dn1)*DTIME
          DECRA(5)=(dn1*A1*QTILD**(dn1-1.D0))*DTIME

      END IF

      RETURN
      END
```

EXAMPLE CREEP.F FILE FOR ZEK100 AT 300 °C

```
      C constitutive equation
      c     de/dt = A1(e)*sigma1^n1(e)+A2*sigma2^n2
      c           A1(e) = exp(-9.97333-12.5909e+17.8488e^2-11.0985e^3)
      c           n1(3) = 1.3325+0.667476tanh(4.6266e)

          SUBROUTINE
     CREEP(DECRA,DESWA,STATEV,SERD,EC,ESW,P,QTILD,
     1
     TEMP,DTEMP,PREDEF,DPRED,TIME,DTIME,CMNAME,LEXIMP,LEND,
     2 COORDS,NSTATV,NOEL,NPT,LAYER,KSPT,KSTEP,KINC)
          INCLUDE 'ABA_PARAM.INC'
          CHARACTER*80 CMNAME
          DIMENSION DECRA(5),DESWA(5),STATEV(*),PREDEF(*),DPRED(*),
     1 TIME(2),EC(2),ESW(2),COORDS(*)

      C-----------------------------------------------------------------+
      C-----------------------------------------------------------------+
      C--------------------------  DECLARATIONS  ------------------------*
      C-----------------------------------------------------------------+
          PARAMETER (dzero=1.D-20)
      C-----------------------------------------------------------------+
      C-----------------------------------------------------------------+
      C------------------  BEGINNING OF EXECUTABLE CODE  ------------------*
      C-----------------------------------------------------------------+
```

```
C-----------------------------------------------------------------------+
C
          A1 = exp(-37.5887-(5.02089*EC(2))
     1 +(17.9394*EC(2)**2)
     1 -(30.2486*EC(2)**3))
          dn1 = 7.9
C-----------------------------------------------------------------------+
C-------- Metal creep: Equivalent (uniaxial) deviatoric creep strain increment.
      DECRA(1)=(A1*QTILD**dn1)*DTIME
C-----------------------------------------------------------------------+
C-------- Metal creep: Derivative
C-------- DECRA(2): D(de^cr)/D(e^cr)
C-------- DECRA(5): D(de^cr)/D(q)

C Calculate the appropriate derivatives of the creep strain increment
      IF(LEXIMP.EQ.1) THEN
      DA1De = A1*(-5.02089+35.8788*EC(2)-90.7458*EC(2)**2)
          DECRA(2)=(DA1De*QTILD**dn1)*DTIME
          DECRA(5)=(dn1*A1*QTILD**(dn1-1.D0))*DTIME

      END IF

      RETURN
      END
```

References

CHAPTER 1

1. "Science Safety: Chapter 8". Government of Manitoba. Retrieved 2007-08-21, “www.edu.gov.mb.ca/k12/docs/support/scisafe/chapter8. html”.
2. A.J. Carpenter, “Physics-Based Material Constitutive Models for the Simulation of High-Temperature Forming of Magnesium Alloy AZ31,” PhD Thesis, University of Texas at Austin, (2012).
3. A.R. Antoniswamy, “The Construction and Use of Physics-Based Plasticity Models and Forming-Limit Diagrams to Predict Elevated Temperature Forming of Three Magnesium Alloy Sheet Materials,” PhD Thesis, University of Texas at Austin, (2013).
4. L.H. Pomeroy: Automotive Engineering, 1922, vol. XI, no. 6, pp. 508-519.
5. G.S. Cole, A.M. Sherman: Mater. Char., 1995, vol. 35, pp. 3-9.
6. J.J. Lee, S.P. Lukachko, I.A. Waitz, A. Schafer: Annual Review of Energy and the Environment, 2001, vol. 26, pp. 167-200.
7. A.I. Taub: *MRS Bulletin*, 2006, vol. 31, pp. 336-343.
8. J.A. Yasi, L.G. Hector, Jr., D.R. Trinkle: *Acta Mater.*, 2011, vol. 59, pp. 5652-60.
9. A.J. Carpenter, A.R. Antoniswamy, J.T. Carter, L.G. Hector, Jr., E.M. Taleff, A Grain-size Dependent Material Constitutive Model for the Hot Deformation of Mg AZ31B Sheet at 450°C, (2014), *Acta Materialia*.

CHAPTER 2

1. S. Kurukuri, D.G. Tari, M.J. Worswick, R.K. Mishra, J.T. Carter, “Dynamic Characterization of AZ31B and ZEK100 Magnesium Alloy Sheets,”

International Conference on Magnesium Alloys and their Applications, W.J. Poole, K.U. Kainer, eds., Vancouver, Canada, 2012.

2. M. Boba, M.J. Worswick, R.K. Mishra, J.T. Carter, "Formability of AZ31B and ZEK100 Magnesium Alloy Sheets at Elevated Temperatures," International Conference on Magnesium Alloys and their Applications, W.J. Poole, K.U. Kainer, eds., Vancouver, Canada, 2012.
3. J. Gao, Q. Wang, Y. Wang, W. Li, W. Niu, "Microstructure and Kinetics of Hot Deformation WE43 Magnesium Alloy," Rare Metals, 27(2008), pp. 405-409.
4. A. Galiyev, R. Kaibyshev, G. Gottstein, "Correlation of Plastic Deformation and Dynamic Recrystallization in Magnesium Alloy ZK60," Acta Materialia, 49(2001), pp. 1199-1207.
5. A. Bussiba, A. Ben Artzy, A. Shtechman, S. Ifergan, M. Kupiec, "Grain Refinement of AZ31 and ZK60 Mg alloys - Towards Superplasticity Studies," Materials Science and Engineering A, 302 (2001), pp. 56-62.
6. A.R. Antoniswamy, "The Construction and Use of Physics-Based Plasticity Models and Forming-Limit Diagrams to Predict Elevated Temperature Forming of Three Magnesium Alloy Sheet Materials," PhD Thesis, University of Texas at Austin, (2013).
7. ASM: Metals Handbook, Vol. 20, Materials Park, OH, 2002.
8. A.J. Carpenter, "Physics-Based Material Constitutive Models for the Simulation of High-Temperature Forming of Magnesium Alloy AZ31," PhD Thesis, University of Texas at Austin, (2012).
9. A.A. Luo: JOM, 2002, vol. 54, no. 2, pp. 42-48.

10. J. Min, Y. Cao, J.T. Carter, R. Verma, “Comparison of Tensile Properties and Crystallographic Textures of Three Magnesium Alloy Sheets,” Magnesium Technology, S.M. Mathaudhu, W.H. Sillekens, N.R. Neelameggham , N.Hort, eds., TMS (2012), pp. 355-360.
11. J. Bohlen, M. R. Nürnberg, J.W. Senn, D. Letzig, S.R. Agnew, “The Texture and Anisotropy of Magnesium–zinc–rare Earth Alloy Sheets,” Acta Materialia, 55 (2007), pp. 2101-2112.
12. M. Boba, M.J. Worswick, R.K. Mishra, J.T. Carter, “Formabiltiy of A31B and ZEK100 Magnesium Alloy Sheets at Elevated Temperatures,” International Conference on Magnesium Alloys and their Applications, W.J. Poole, K.U. Kainer, eds., Vancouver, Canada, 2012.
13. 13. M.W. Toaz, E.J. Ripling: J. Met., 1956, vol. 8, pp. 936-946.Birbilis, N.; Williams, G.; Gusieva, K.; Samaniego, A.; Gibson, M. A.; McMurray, H. N. (2013). "Poisoning the corrosion of magnesium". Electrochemistry Communications 34: 295. doi:10.1016/j.elecom.2013.07.021
14. G.S. Cole, A.M. Sherman: Mater. Char., 1995, vol. 35, pp. 3-9.
15. "Science Safety: Chapter 8". Government of Manitoba. Retrieved 2007-08-21.
16. H.-K. Kim, W.-J. Kim, Creep Behavior of AZ31 Magnesium Alloy at Low Temperature Range between 423 K and 473 K, J. Mater. Sci., 2007, 42(15) , pp. 6171-6176.
17. I.A. Maksoud, H. Ahmed, J. Rödel, Investigation of the Effect of Strain Rate and Temperature on the Deformability and Microstructure Evolution of AZ31 Magnesium Alloy, Mater. Sci. Eng. A, 2009, 504(1), pp. 40-48.

18. S. Spigarelli, M. El Mehtedi, Creep as an Extension of Hot Working: A Unified Approach to High Temperature Deformation of AZ31 Alloy, Mater. Sci. Eng. A, 2010, 527(21), pp. 5708-5714.
19. C. Bruni, L. Donati, M. El Mehtedi, M. Simoncini, Constitutive Models for AZ31 Magnesium Alloys, Key Eng. Mater., 2008, 367, pp. 87-94.
20. U.F. Kocks, C.N. Tome, H.-R. Wenk (Eds.), "Texture and Anisotropy," Cambridge, New York (2000), pp. 204-206.
21. P.A. Sherek, A.J. Carpenter, L.G. Hector, Jr., P.E. Krajewski, J.T. Carter, J. Lasceski, E.M. Taleff, "The Effects of Strain and Stress State in Hot Forming of Mg AZ31 Sheet," *Magnesium Technology*, S.M. Mathaudhu, W.H. Sillekens, N.R. Neelameggham , N.Hort, eds., TMS (2012), pp. 301-306.
22. Alexander J. Carpenter, Eric M. Taleff, Louis G. Hector, Jr., Jon T. Carter, and Paul E. Krajewski. "A Time-Dependent Material Model for the Simulation of Hot Gas-Pressure Forming of Magnesium Alloy AZ31." *Materials Science Forum*, 735 (2013), pp. 198-203.
23. E.M. Taleff, L.G. Hector, Jr., R. Verma, P.E. Krajewski, J.-K. Chang: J. Mater. Eng. Perform., 2010, vol. 19, pp. 488-94.
24. F.K. Abu-Farha, M.K. Khraisheh: Adv. Eng. Mater., 2007, vol. 9, no. 9, pp. 777-83.
25. J. Min, J. Lin: Anelastic Behavior and Phenomenological Modelling of Mg ZEK100-O Alloy Sheet Under Cyclic Tensile Loading – Unloading, Mater. Sci. Eng. A, 2013, pp. 174 – 182.
26. I. Aslam, B. Li, Z. McClelland, S.J. Horstemeyer, Q. Ma, P.T. Wang, M.F. Horstemeyer: Three Point Bending Behavior of a ZEK100 Mg Alloy at Room Temperature, Mater. Sci. Eng. A 590, pp. 168-173.

27. J. Min, J. Lin, J. Li: Forming Limits of Mg Alloy ZEK100 Sheet in Perform Annealing Process, (2013).
28. M. Alderman: The Lightest Structural Metal in Automotive, Niche Vehicle Network, (2013).

CHAPTER 3

1. A.J. Carpenter, "Physics-Based Material Constitutive Models for the Simulation of High-Temperature Forming of Magnesium Alloy AZ31," PhD Thesis, University of Texas at Austin, (2012).
2. A.R. Antoniswamy, "The Construction and Use of Physics-Based Plasticity Models and Forming-Limit Diagrams to Predict Elevated Temperature Forming of Three Magnesium Alloy Sheet Materials," PhD Thesis, University of Texas at Austin, (2013).

CHAPTER 4

1. J. Min, J. Lin: Anelastic Behavior and Phenomenological Modelling of Mg ZEK100-O Alloy Sheet Under Cyclic Tensile Loading – Unloading, Mater. Sci. Eng. A, 2013, pp. 174 – 182.
2. H. M. Rao, R. I. Rodrigez, J. B. Jordon, M. E. Barkey, Y. B. Guo, H. Badarinarayan, W. Yuan, Friction Stir Spot Welding of Rare-Earth Containing ZEK100 Magnesium Alloy Sheets, Material and Design 56 (2014), pp. 750-754.
3. A.R. Antoniswamy, "The Construction and Use of Physics-Based Plasticity Models and Forming-Limit Diagrams to Predict Elevated Temperature Forming of Three Magnesium Alloy Sheet Materials," PhD Thesis, University of Texas at Austin, (2013).

4. A.J. Carpenter, “Physics-Based Material Constitutive Models for the Simulation of High-Temperature Forming of Magnesium Alloy AZ31,” PhD Thesis, University of Texas at Austin, (2012).
5. R.R. Craig, Jr.: Mechanics of Materials, 3rd ed., Hoboken: John Wiley & Sons, 2011, pp. 37-45.
6. G.I. Taylor: J. Inst. Metals, 1938, vol. 62, pp. 307–24.

CHAPTER 5

1. A.R. Antoniswamy, “The Construction and Use of Physics-Based Plasticity Models and Forming-Limit Diagrams to Predict Elevated Temperature Forming of Three Magnesium Alloy Sheet Materials,” PhD Thesis, University of Texas at Austin, (2013).
2. S.L. Robinson, O.D. Sherby, Mechanical Behavior of Polycrystalline Tungsten at Elevated Temperature, Acta Metall., 17(2), 1969, pp. 109-125
3. O.A. Ruano, A.K. Miller, O.D. Sherby, The Influence of Pipe Diffusion on the Creep of Fine-grained Materials, Mater. Sci. Eng., 51(1), 1981, pp. 9-16.
4. K. Hantzsche, J. Wendt, K.U. Kainer, J. Bohlen, D. Letzig, Mg Sheet: The Effect of Process Parameters and Alloy Composition on Texture and Mechanical Properties, JOM, 61(8), 2009, p 38-42.

CHAPTER 6

1. A.R. Antoniswamy, “The Construction and Use of Physics-Based Plasticity Models and Forming-Limit Diagrams to Predict Elevated Temperature Forming of Three Magnesium Alloy Sheet Materials,” PhD Thesis, University of Texas at Austin, (2013).

2. S.L. Robinson, O.D. Sherby, Mechanical Behavior of Polycrystalline Tungsten at Elevated Temperature, Acta Metall., 17(2), 1969, pp. 109-125
3. O.A. Ruano, A.K. Miller, O.D. Sherby, The Influence of Pipe Diffusion on the Creep of Fine-grained Materials, Mater. Sci. Eng., 51(1), 1981, pp. 9-16.
4. S. R. Agnew, O. Duygulu, "Plastic Anisotropy and the Role of Non-basal Slip in Magnesium Alloy AZ31B," International Journal of Plasticity, 21 (2005), pp. 1161-1193.
5. J. Koike, R. Ohyama, T. Kobayashi, M. Suzuki and K. Maruyama, "Grain-Boundary Sliding in AZ31 Magnesium Alloys at Room Temperature to 523K," Materials Transactions, 44 (2003), pp. 445-451.
6. W. Köster, "Die Temperaturabhängigkeit des ElisatizitätsmodulsreinerMetalle," Zeitschriet für Metallkunde, 39 (1948), pp. 1–9.
7. O.A. Ruano, A.K. Miller, O.D. Sherby, The Influence of Pipe Diffusion on the Creep of Fine-grained Materials, Mater. Sci. Eng., 51(1), 1981, pp. 9-16.
8. H.J. Frost, M.F. Ashby," Deformation Mechanism Map", Pergamon Press, Elmsford, NY, (1982), p 44.
9. Y. Jia, "Hot deformation behavior of spray-deposited Al–Zn–Mg–Cu alloy", Materials and Design, (2014), p 79-85.
10. H.-K. Kim, W.-J. Kim, Creep Behavior of AZ31 Magnesium Alloy at Low Temperature Range between 423 K and 473 K, J. Mater. Sci., 2007, 42(15) , pp. 6171-6176.
11. I.A. Maksoud, H. Ahmed, J. Rödel, Investigation of the Effect of Strain Rate and Temperature on the Deformability and Microstructure Evolution of AZ31 Magnesium Alloy, Mater. Sci. Eng. A, 2009, 504(1), pp. 40-48.

12. S. Spigarelli, M. El Mehtedi, Creep as an Extension of Hot Working: A Unified Approach to High Temperature Deformation of AZ31 Alloy, Mater. Sci. Eng. A, 2010, 527(21), pp. 5708-5714.
13. C. Bruni, L. Donati, M. El Mehtedi, M. Simoncini, Constitutive Models for AZ31 Magnesium Alloys, Key Eng. Mater., 2008, 367, pp. 87-94.
14. K.E. Tello, A.P. Gerlich, P.F. Mendez, Constants for Hot Deformation Constitutive

    Models for Recent Experimental Data, Sci. Technol. Weld. Joining, 2010, 15(3), pp. 260-266.
15. A.J. Carpenter, Physics-Based Material Constitutive Models for the Simulation of High-Temperature Forming of Magnesium Alloy AZ31, PhD Thesis, University of Texas at Austin, (2012).
16. P.A. Sherek, Simulation and Experimental Investigation of Hot Gas-Pressure Forming for Light-Alloy Sheet Material, Thesis, Mechanical Engineering, The University of Texas at Austin, 2009.
17. P.A. Sherek, A.J. Carpenter, L.G. Hector, Jr., P.E. Krajewski, J.T. Carter, J. Lasceski, E.M. Taleff, The Effects of Strain and Stress State in Hot Forming of Mg AZ31 Sheet, Magnesium Technology, Wiley, 2012, pp. 301-306.
18. O. D. Sherby, P. M. Burke, Mechanical Behavior of Crystalline Solid at Elevated Temperature, Acta Metall., 1968, pp. 325-386

CHAPTER 7

1. J.W. Backus: FORTRAN 77, Armonk: IBM, 1978.

2. A.J. Carpenter, “Physics-Based Material Constitutive Models for the Simulation of High-Temperature Forming of Magnesium Alloy AZ31,” PhD Thesis, University of Texas at Austin, (2012).
3. A.R. Antoniswamy, “The Construction and Use of Physics-Based Plasticity Models and Forming-Limit Diagrams to Predict Elevated Temperature Forming of Three Magnesium Alloy Sheet Materials,” PhD Thesis, University of Texas at Austin, (2013).
4. P.A. Sherek, “Simulation and Experimental Investigation of Hot Gas-Pressure Forming for Light-Alloy Sheet Material, Thesis, Mechanical Engineering,” Master Thesis, University of Texas at Austin, (2009).